Genuinely third-order advection scheme for atmospheric flows : the Multidimensional Positive Definite Advection Transport Algorithm approach

Maciej Waruszewski

A doctoral dissertation
prepared at the Institute of Geophysics,
Faculty of Physics, University of Warsaw

under the supervision of
Professor Hanna Pawłowska

Warsaw, December 2018

Contents

Acknowledgements

First, I would like to thank my supervisor prof. Hanna Pawłowska for her support, encouragement and kindness. I am particularly grateful for allowing me to pursue research aligned with my own interests and abilities. Equally important was mentoring by prof. Piotr Smolarkiewicz, who suggested the initial research topic and guided me in every aspect of the work, from the beginning to the very end. This thesis could not be completed without his insightful comments and readiness to share his vast knowledge. Additionally, I benefited from his many anecdotes and sage advice. Parts of this work were completed during my visits to the European Centre for Medium-Range Weather Forecasts (ECMWF). I would like to thank the centre's staff for their hospitality and personally thank dr Christian Kühnlein for his encouragement and useful discussions while preparing the journal article that forms the basis of the thesis.

The thesis was prepared at the Institute of Geophysics, where I was surrounded by great colleagues and helpful staff. As a member of the cloud modelling research group, I enjoyed the company of Dorota Jarecka, Sylwester Arabas, Anna Jaruga, Piotr Dziekan and Gustavo Abade. I would like to extend special thanks to Anna Jaruga for helping me with the practicalities of graduate studies and to Sylwester Arabas for installing in me some of his zeal for open software and open science.

I am grateful to my parents, Elżbieta and Grzegorz, for their unwavering belief in me and for helping with mundane matters. My frequent visits to their home gave me a much needed breathing space, and left me reinvigorated every time.

I would like to acknowledge the work of developers of the free and open-source software used in the preparation of the thesis.

This work was partly funded by the Polish National Science Centre (decision numbers: 2012/06/M/ST10/00434 and 2016/23/B/ST10/00690). Visits to ECMWF were partially funded by the European Research Council under the European Union's Seventh Framework Programme (FP/2012/ERC Grant agreement no. 320375).

Abstract

Numerical modelling of the atmosphere is crucially important for the state-of-the-art weather forecasting and climate prediction. In weather, climate, and chemistry-transport models, advective transport of moist air, chemical species, or pollutants has to be represented with high accuracy. Furthermore, advection schemes need to respect the fundamental physical principles of transport, such as conservation, monotonicity, compatibility with mass continuity, and correlations between tracers.

Numerical errors and behavioural properties of an advection scheme are dependent on its order of accuracy. In atmospheric modelling, second-order accurate schemes are common, and a trend towards high-order (i.e. third-order or higher) accurate algorithms can be observed. However, combining high-order accuracy with robustness and physical realisability is far from trivial.

To achieve high-order accuracy without compromising advantageous numerical properties, this thesis proposes a third-order accurate advection scheme based on the Multidimensional Positive Definite Advection Transport Algorithm (MPDATA). MPDATA-based solvers have a rich history of successful applications in geo- and astrophysics. The standard MPDATA advection scheme is second-order accurate, sign-preserving (optionally nonoscillatory), and fully multidimensional. Remarkably, in simulations of turbulent flows, MPDATA can provide an implicit subgrid-scale turbulence model.

This thesis extends MPDATA to third-order accuracy for temporally or spatially varying flows, while preserving its beneficial characteristics. This is accomplished by deriving the leading truncation error of the standard second-order MPDATA, performing the Cauchy-Kowalevski procedure to express it in a spatial form and compensating its discrete representation—much in the same way as the standard MPDATA corrects the first-order accurate upwind scheme. The procedure of deriving the spatial form of the truncation error was automated using a computer algebra system. This enables various options in MPDATA to be included straightforwardly in the third-order scheme, thereby minimising the implementation effort in existing code bases. Following the spirit of MPDATA, the error is compensated using the upwind scheme resulting in a sign-preserving algorithm, and the entire scheme can be formulated using only two upwind passes. Established MPDATA enhancements, such as formulation in generalised

curvilinear coordinates, the nonoscillatory option or the infinite-gauge variant, carry over to the fully third-order accurate scheme.

The novel scheme was implemented in *libmpdata++*, which is an open-source library of MPDATA-based solvers. Highlights of the library are presented, particularly stressing its design based on object-oriented programming and modern software development practices. Benefits of the adopted design choices for implementing the fully third-order accurate scheme are discussed.

A manufactured 3D analytic solution is used to verify the theoretical development and its numerical implementation. Global tracer-transport benchmarks facilitate comparison of the fully third-order accurate MPDATA to other schemes popular in computational meteorology, while also demonstrating its benefits for chemistry-transport models fundamental to air quality monitoring, forecasting and control.

Advantages of the fully third-order-accurate MPDATA for fluid dynamics applications are illustrated by simulations of a double shear layer, a convective boundary layer, and an idealised supercell storm. The double shear layer simulations quantify the increased accuracy of the new scheme in an overall lower-order accurate flow solver. Simulations of the convective boundary layer reveal its implicit subgrid-scale turbulence model. Characteristics of the scheme in simulations with parametrised cloud microphysics are explored in the idealised supercell storm benchmark.

Using the genuinely third-order accurate MPDATA consistently improved simulation results in a variety of test cases relevant to atmospheric modelling. The improvement was especially significant for the tracer transport benchmarks; therefore, the novel scheme can be generally recommended for tracer transport applications. In simulations of turbulent flows, the fully third-order accurate MPDATA revealed an implicit subgrid-scale model with beneficial characteristics. An increased complexity of the new scheme is offset by the availability of its open-source implementation.

Streszczenie

Modelowanie numeryczne jest ważnym, jeśli nie najważniejszym, narzędziem wykorzystywanym w prognozowaniu pogody oraz predykcjach klimatycznych. W modelach pogody, klimatu i transportu zanieczyszczeń adwekcyjny transport powietrza, związków chemicznych lub zanieczyszczeń powinien być opisany z dużą precyzją. Co więcej, schematy adwekcyjne muszą respektować fundamentalne prawa fizyczne, takie jak zachowawczość, monotoniczność i korelacje pomiędzy transportowanymi składnikami.

Własności i błędy numeryczne schematu adwekcyjnego zależą od jego rzędu dokładności. W modelowaniu atmosfery powszechnie stosowane są schematy drugiego rzędu dokładności. Ostatnio daję się jednak zaobserwować trend ku algorytmom wyższego rzędu dokładności (tj. trzeciego lub wyższego). Połączenie wysokiego rzędu dokładności ze stabilnością schematu i respektowaniem praw fizycznych jest nietrywialne.

Niniejsza praca proponuje schemat adwekcyjny trzeciego rzędu dokładności w oparciu o istniejący algorytm MPDATA (Multidimensional Positive Definite Advection Transport Algorithm). Modele oparte o schemat MPDATA mają bogatą historię zastosowań w geo- i astrofizyce. Standardowy schemat adwekcyjny MPDATA jest drugiego rzędu dokładności, zachowuje znak (opcjonalnie jest nieoscylacyjny) i jest w pełni wielowymiarowy. Warto podkreślić, że w symulacjach przepływów turbulentnych MPDATA może modelować w niejawny sposób turbulencję podskalową.

Niniejsza praca rozszerza algorytm MPDATA do trzeciego rzędu dokładności dla przepływów zmiennych w czasie lub przestrzeni, jednocześnie utrzymując wszystkie zalety istniejących schematów MPDATA o drugim rzędzie dokładności. Zostało to osiągnięte przez wyprowadzenie wiodącego członu błędu obcięcia standardowego schematu MPDATA drugiego rzędu, przeprowadzenie procedury Cauchy-Kowalewskiej w celu wyrażenia go w formie przestrzennej i kompensacje jego dyskretnej postaci—w sposób bardzo podobny do tego jak standardowy schemat MPDATA poprawia błąd schematu pierwszego rzędu dokładności typu upwind. Procedura wyprowadzenia błędu obcięcia w formie przestrzennej została zautomatyzowana poprzez użycie systemu algebry komputerowej. Pozwala to na uwzględnienie różnych opcji algorytmu MPDATA bezpośrednio w schemacie trzeciego rzędu dokładności, ułatwiając w ten sposób implementacje algorytmu w istniejących kodach komputerowych. W duchu algorytmu MPDATA, błąd jest kompensowany używając schematu typu upwind, co skutkuje otrzymaniem algorytmu

zachowującego znak, oraz wymagającym jedynie dwóch iteracji typu upwind. Różne opcje algorytmu MPDATA (takie jak: wersja w uogólnionych zmiennych krzywoliniowych lub opcja nieoscylacyjna) w sposób prosty mogą być zastosowane w schemacie o pełnym trzecim rzędzie dokładności.

Nowy schemat został zaimplementowany w bibliotece schematów MPDATA z otwartym kodem źródłowym, *libmpdata++*. W pracy przedstawiono główne idee przyświecające stworzeniu biblioteki, szczególnie podkreślając jej zamysł oparty na programowaniu obiektowym oraz użyciu nowoczesnych zasadach inżynierii oprogramowania. Przedyskutowana są zalety takiego zaprojektowania biblioteki dla implementacji schematu o pełnym trzecim rzędzie dokładności.

Specjalnie skonstruowane trójwymiarowe rozwiązanie równania adwekcji jest użyte w celu weryfikacji teoretycznego wyprowadzenia oraz jego numerycznej implementacji. Standardowe testy transportu adwekcyjnego pozwalają na porównanie nowego schematu z innymi popularnymi schematami stosowanymi w meteorologii obliczeniowej. Demonstrują również jego zalety dla modeli transportu zanieczyszczeń używanych do monitorowania, prognozy, i kontroli jakości powietrza.

Zalety schematu MPDATA o pełnym trzecim rzędzie dokładności dla zastosowań w dynamice płynów są zilustrowane poprzez symulacje podwójnej warstwy ścinania, konwekcyjnej warstwy granicznej oraz wyidealizowanej superkomórki burzowej. W symulacjach podwójnej warstwy ścinania przeprowadzona została ilościowa analiza zwiększonej dokładności nowego schematu w modelu, który jako całość ma mniejszy rząd dokładności. Symulacje konwekcyjnej warstwy granicznej pokazują niejawny model turbulencji podskalowej nowego schematu MPDATA. Cechy schematu w symulacjach z parametryzowaną mikrofizyką chmur zostały zbadane w teście wyidealizowanej superkomórki burzowej.

Podsumowując, użycie schematu MPDATA o trzecim rzędzie dokładności poprawiło wyniki symulacji w różnych testowanych przypadkach istotnych w modelowaniu atmosfery. Zalety nowego schematu są szczególnie dobrze widoczne w standardowych testach transportu adwekcyjnego, , zatem używanie go dla rozwiązywania transportu adwekcyjnego może być szczerze rekomendowane. Nowy algorytm MPDATA, lepiej niż jego wersja standardowa, modeluje w niejawny sposób turbulencję podskalową. Skomplikowaność nowego schematu nie stanowi dużego problemu dzięki dostępności jego otwartej implementacji.

1 Introduction

The Earth's atmosphere is a complex system composed of moist air and a multitude of trace chemical species evolving on a variety of spatio-temporal scales. While fluid dynamics and thermodynamics are believed to provide adequate mathematical description, obtaining a solution to the governing equations generally necessitates the use of numerical methods. Advection is one of the fundamental processes in fluids and hence its numerical representation is of the utmost importance in the design of numerical models of the atmosphere. Numerical advection schemes are at the heart of long-range chemistry-transport models with applications to monitoring, forecasting and control of air pollution. In dynamical models advective terms form the principal nonlinearity of atmospheric equations of motion, and are responsible for such phenomena as energy cascades and turbulence.

Since the advent of numerical atmospheric modelling the simultaneous increase in computing power and algorithms' sophistication have enabled realistic transient three-dimensional simulations. However, the current computing resources are still far from allowing sufficient resolution of the full range of atmospheric scales. Therefore, minimising numerical errors by the use of advanced algorithms is still critical. Moreover, it is increasingly necessary to develop algorithms suitable for contemporary massively parallel machines. An advection scheme is a part that faces the most stringent accuracy requirements and is usually responsible for a sizeable part of the run time. Consequently, there is a continuing quest for improved advection schemes applied in climate, weather and chemistry-transport models.

Numerical modelling of advection in atmospheric flows is challenging because of the highly variable multi-scale circulations and the need to respect the fundamental physical properties of transport. For example, compatibility with mass continuity is vital but is not automatically assured when combining different discretisations (Gross et al., 2002). Conservation of mass is important for transport of moisture or long-lived reactive species, especially for long-term climate simulations. Preservation of other analytically conserved quantities may be beneficial for specialised applications (Thuburn, 2008). While atmospheric flows are characterised by low Mach numbers and do not develop shocks, regions of sharp gradients in transported variables frequently occur—consider for example atmospheric fronts or a cloud-air interface—and have to be captured accurately.

To avoid overshoots or undershoots near large gradients, schemes that are monotonicity preserving are preferable. Representations of moist processes or chemical reactions do not tolerate negative values, making sign preservation a paramount property. Some tracer mixing ratios (for example nitrous oxide N_2O and 'total odd nitrogen' NO_y) appear to be related by simple functional relations, in that case it is advantageous that a transport scheme does not disturb their correlations. To allow quasi-uniform distributions of mesh points on the sphere or to handle the orography, advection schemes should be geometrically flexible; either by incorporating coordinate transformations, or formulations on unstructured meshes. Finally, good performance and scalability on modern machines with high core counts is essential. All together, balancing accuracy, efficiency and the physical realisability is problem specific and rarely straightforward.

The key properties of a finite-difference approximation to any properly posed initial value problem are (in the spirit of the Lax's Equivalence Theorem) the consistency, stability and convergence (§3 in Richtmyer and Morton (1967), §13.2 in Toro (2009)). The first two are necessary for the third that per se is a categorical imperative of computational physics. Inherent in the concept of convergence are the interrelated notions of the convergence rate and truncation error, epitomised by the order of accuracy. The latter is a simple single measure that reflects the dependence of the approximation's leading truncation error on the powers of the discretisation increments (spatial or temporal, or both) as well as the asymptotic rate at which the approximate solution converges to the sufficiently smooth genuine result in terms of the increments' powers as they tend to zero; cf. §7 in Richtmyer and Morton (1967). While high-order accuracy is a holy grail of numerical analysis, designing even a truly second-order method for practical problems of computational physics can be a difficult (if at all attainable) task; see Knoll et al. (2003), §20.5.2 in Toro (2009) and Jarecka et al. (2015) for related discussions. Moreover, for complex computational models solving systems of inhomogeneous partial differential equations (PDEs) with multiplicity of the right-hand-side (rhs) forcings that act on disperse spatio-temporal scales, the asymptotic convergence rate may be practically inaccessible even though the employed method is formally sufficiently accurate. This, however, does not preclude the utility of high-order approximations, because the actual functional form of the leading truncation error can determine behavioural errors (such as excessive implicit diffusion or dispersion, lack of conservation or sign preservation, etc.), which for the application at hand can be more important than the formal accuracy (§III-A-23 in Roache (1972)).

Historically, the first-order-accurate advection schemes were discarded due to the notorious implicit diffusion, stimulating the development of second-order-accurate schemes. However, already in the seventies, higher-order schemes (i.e. third-order or higher) were shown to have computational advantages for atmospheric applications (Kreiss and Oliger, 1972). The key motivation is that higher-order accuracy can be more cost-effective than increasing resolution with a lower-order scheme, but there can

be others related to the behavioural errors; e.g., a more uniform accuracy in terms of the Courant number and better preservation of the solution symmetries (Jaruga et al., 2015), or the strong stability at reduced dissipativity (see §5.4 in Richtmyer and Morton (1967) for a substantive discussion). More recent studies demonstrated the efficiency of higher-order methods in the area of computational fluid dynamics (Wang et al., 2013) and in representing atmospheric wave motion (Ullrich, 2014), while a trend towards higher-order schemes can be observed for atmospheric modelling (Ullrich and Jablonowski, 2012; Kelly and Giraldo, 2012; Skamarock et al., 2012). It is worth noting that, even though the literature on high-order advection schemes is vast, many formulations adopt simplifying assumptions of constant velocity and may not reach their target accuracy for variable flows. Additionally, many very high-order methods are only formulated for one dimensional advection, and when used in a dimensionally-split fashion (Strang, 1968), only achieve second-order accuracy in multidimensional applications (§4.3 in Gustafsson et al. (1995)).

This thesis concerns construction, verification and application of a genuinely (i.e. for variable flows and in multiple dimensions) third-order advection scheme following the approach of Multidimensional Positive Definite Advection Transport Algorithm (MPDATA), a method proven in geophysical applications. The material is based in-part on Waruszewski et al. (2018), extended with additional details, discussions, and simulations.

The MPDATA scheme and MPDATA-based flow-solvers have a rich history. As it stands today, the term MPDATA encompasses a class of generally second-order accurate nonoscillatory forward-in-time[1] advection algorithms, formulated as finite-difference (FD) schemes on structured rectilinear grids (Smolarkiewicz, 1984; Smolarkiewicz and Margolin, 1998) or finite-volume (FV) schemes on unstructured meshes (Smolarkiewicz and Szmelter, 2005; Kühnlein and Smolarkiewicz, 2017). MPDATA schemes are based on iterative application of the first-order accurate upwind scheme, while exploiting its sign-preserving property (Smolarkiewicz, 1984). In the first pass the transported variable is advected by the physical velocity, whereas subsequent passes use error-compensating pseudo-velocities designed to compensate the leading-order spatial and temporal truncation errors of the upwind scheme. Only one corrective pass is required for the second-order accuracy. MPDATA schemes have many virtues, including full multidimensionality, conservation, sign-preservation, nonlinear stability and relatively small phase error (Smolarkiewicz and Margolin, 1998; Smolarkiewicz and Szmelter, 2005). Sign-preservation can be extended to monotonicity by means of the nonoscillatory option (Smolarkiewicz and Grabowski, 1990). The nonoscillatory option is typically combined with the infinite-gauge (asymptotic limit of MPDATA for an infinite constant background), especially suitable for the transport of variable-sign

[1] Temporal derivatives are approximated with forward-in-time differences, while temporal errors are compensated by utilising the information contained in the governing PDE.

fields and having favourable efficiency.

In order to guarantee the second-order accuracy in time, the pseudo-velocities of MPDATA contain terms compensating the error of the forward-in-time differencing. This places MPDATA in a class of one-step Lax-Wendroff schemes (Lax and Wendroff, 1960), that use the Cauchy-Kowalevski procedure (Toro, 2009) to transform temporal derivatives in the error terms into spatial derivatives while relying on the structure of the governing PDEs. Advantages of forward-in-time methods include the reduced storage requirements compared to multi-level schemes and the absence of computational modes such as those typical of basic centred-in-time schemes. The Cauchy-Kowalevski procedure was also instrumental for transforming MPDATA into a family of solvers for generalised transport equations with arbitrary right-hand-sides in curvilinear coordinates (Smolarkiewicz and Margolin, 1993, 1998). Recent advances comprise soundproof-time-step semi-implicit integration schemes for the compressible Euler equations of all-scale atmospheric dynamics based on the FD (Smolarkiewicz et al., 2014) and the FV (Kühnlein and Smolarkiewicz, 2017) MPDATA formulations.

Simulations of high Reynolds number flows with the nonoscillatory MPDATA revealed that, in the absence of an explicit subgrid-scale turbulence model, the scheme itself provides an implicit subgrid-scale model (Margolin et al., 1999). While it is not surprising that the truncation error of a conservative scheme forms an effective stress tensor, the veracity of the approach, dubbed implicit large-eddy-simulation (ILES), is remarkable. The ILES property was subsequently studied in depth (Margolin et al., 2002; Margolin and Rider, 2002; Domaradzki et al., 2003; Margolin et al., 2006b,a; Strugarek et al., 2016) and verified in diverse geo- and astrophysical applications (Warn-Varnas et al., 2007; Prusa et al., 2008; Piotrowski et al., 2009; Ghizaru et al., 2010; Racine et al., 2011; Kumar et al., 2015). ILES is particularly suitable for problems where formulating physically motivated subgrid-scale turbulence models is hard, for example when subgrid scales are anisotropic or when complicated coordinate transformations are applied. In Margolin and Rider (2002); Margolin et al. (2006a) the ILES property was attributed to the similarity between the truncation terms of the basic MPDATA and the finite-scale corrections to the Burgers's and Navier Stokes's equations. At first glance, this suggests that going beyond the second-order accuracy may impact the scheme suitability for ILES. However, the ILES property can be also realised via the nonoscillatory enhancement of the infinite-gauge option (Margolin et al., 1999; Domaradzki et al., 2003; Margolin et al., 2006b), or the basic MPDATA truncation combined with the nonoscillatory enhancement (Warn-Varnas et al., 2007; Ghizaru et al., 2010; Racine et al., 2011; Strugarek et al., 2016; Cossette et al., 2017). All three options have merits benefiting specialised applications. The specific question of suitability of the fully third-order accurate MPDATA for ILES is addressed in the thesis.

The FD-MPDATA is the basis of the EULAG model (Prusa et al., 2008; Smolarkiewicz and Charbonneau, 2013) , while the FV-MPDATA is employed in the Finite-Volume

Module (FVM) for global all-scale atmospheric flows (Smolarkiewicz et al., 2016, 2017; Kühnlein et al., 2018). Recently, the FD-MPDATA based solvers were also implemented in an open-source free/libre library *libmpdata++* (Jaruga et al., 2015), of which the author of the thesis is one of core developers. The aim of the library is to provide a set of reusable components for building MPDATA-based numerical models, while strictly adhering to the modern software-development practices such as automatic testing, clear separation of concerns, and focus on readability and maintainability. Together with it's sister cloud microphysics library *libcloudph++* (Arabas et al., 2015), *libmpdata++* serves as the basis of University of Warsaw Lagrangian Cloud Model (UWLCM), a LES model for researching microphysical effects in warm clouds.

Technically, the proposed scheme can be viewed as an extension of the work in Margolin and Smolarkiewicz (1998), where a recursively summed error-compensating pseudo-velocity was derived and a third-order accurate FD-MPDATA was devised under the assumption of a constant physical velocity. To obtain the third-order accuracy two sources of error had to be compensated, the truncation error of the upwind scheme and the MPDATA corrective pass. The error was compensated by either using the recursive pseudo-velocity (resulting in a scheme with just one corrective iteration) or performing two corrective iterations. For problems where the velocity field changes in space or time, this variant of MPDATA is formally second-order accurate but, nonetheless, offers improved accuracy and diminishes the error dependence on the Courant number.

Here, an extension of the FD-MPDATA to the third-order accuracy for variable flows is presented. In contrast with Margolin and Smolarkiewicz (1998), the full truncation error of the second-order FD-MPDATA is analytically derived, rather than solely the error of the first upwind pass. The error is then transformed into a spatial form following the Cauchy-Kowalevski procedure. The leading order-truncation error is written as a pseudo-velocity, and the origins of the terms that compose it are discussed. The adopted approach has the advantage that a two-pass third-order accurate scheme can be easily constructed, obviating the need for the recursive pseudo-velocity. Furthermore, established MPDATA enhancements, such as formulation in generalised curvilinear coordinates, the nonoscillatory option or the infinite-gauge variant, carry over to the fully third-order accurate scheme.

For verifying the correctness of the analytic derivations as well as their numerical implementation, a manufactured 3D analytic solution is used, designed to have the full coordinate dependence of the advective velocity. To provide an example of intermediate complexity that is both relevant to atmospheric applications and facilitates comparisons to other advection algorithms popular in computational meteorology, two standard test cases for tracer transport in spatially variable time-dependent flows on the sphere are adopted. The first is the moving vortices on the sphere test case from Nair and Jablonowski (2008). The second is selected from the test suite in Lauritzen et al. (2012), and addresses tracer correlations in a reversing deformational flow.

Having proved the newly developed advection scheme, its advantages to simulate fluid dynamics are demonstrated. Simulations of a viscous double shear layer rollup (Drikakis and Smolarkiewicz, 2001; Drikakis et al., 2002) discriminately quantify the benefit of the fully third-order MPDATA embedded in a lower-order accuracy flow solver. Similarly, simulations of a dry convective boundary layer (Margolin et al., 1999) illustrate the scheme advantages in simulations of atmospheric flows, while also addressing its suitability for implicit large-eddy simulations. Finally, the performance and robustness of the proposed scheme are explored in simulations of an idealised supercell storm, a complex atmospheric benchmark case featuring very strong winds, small-scale microphysical effects and heavy precipitation.

The thesis is organised as follows. In Chapter 2 the standard FD-MPDATA scheme for the solution of a homogeneous generalised transport equation is outlined. Chapter 3 contains the novel truncation error analysis of the standard FD-MPDATA, constructs the fully third-order accurate MPDATA, and provides details of its implementation. Chapter 4 provides an overview of the *libmpdata++* library of MPDATA solvers, which contains an open implementation of the scheme and was used to perform simulations presented in the thesis. The proposed scheme is first verified and compared to the established MPDATAs based on tracer transport benchmarks in Chapter 5. Afterwards, Chapter 6 demonstrates the utility of the fully third-order-accurate MPDATA for fluid dynamics simulations, including ILES study of three-dimensional turbulent atmospheric flow. Idealised supercell simulations are presented in Chapter 7. Chapter 8 presents conclusions and final remarks. Some technical details and derivations are delegated to appendices.

2 Standard MPDATA

This chapters reviews the standard MPDATA scheme—first introduced in Smolarkiewicz (1983) and subsequently extended—for integrating the homogeneous generalised transport equation

$$\frac{\partial G\Psi}{\partial t} + \nabla \cdot (\boldsymbol{V}\Psi) = 0 \ , \tag{2.1}$$

where $\Psi(t, \boldsymbol{x})$ is a scalar field and $(t, \boldsymbol{x})$ are the independent curvilinear coordinates. The symbol $\nabla\cdot$ represents the scalar product of the nabla operator $\nabla = (\partial_x, \partial_y, \partial_z)$ with a vector. In general, the symbol G corresponds to the Jacobian of the coordinate transformation, the fluid density, or a product of both. Hereafter, it is assumed that G is independent of time $G = G(\boldsymbol{x})$. The vector field $\boldsymbol{V} = G\dot{\boldsymbol{x}}$ denotes a generalised flow field, where $\dot{\boldsymbol{x}}$ is the contravariant velocity in the underlying coordinate system.

The presentation follows in-part already available comprehensive reviews (Smolarkiewicz and Margolin, 1998; Smolarkiewicz, 2006) with the aim of providing the necessary background for the next chapter introducing the fully third-order-accurate scheme.

2.1 Derivation in 1D

To explain the underlying idea behind MPDATA in a simplified setting consider (2.1) in one dimension, with $U := V^1$,

$$\frac{\partial \Psi}{\partial t} + \frac{1}{G}\frac{\partial}{\partial x}(U\Psi) = 0. \tag{2.2}$$

The first-order upwind approximation to (2.2) is written in the flux form

$$\Psi_i^{n+1} = \Psi_i^n - \frac{1}{G_i}\left[F(\Psi_i^n, \Psi_{i+1}^n, \mathcal{U}_{i+1/2}) - F(\Psi_{i-1}^n, \Psi_i^n, \mathcal{U}_{i-1/2})\right], \tag{2.3}$$

where

$$F\left(\Psi_L, \Psi_R, \mathbb{V}\right) = 0.5\left[(|\mathbb{V}| + \mathbb{V})\Psi_L + (\mathbb{V} - |\mathbb{V}|)\Psi_R\right] \tag{2.4}$$

is the upwind flux function. Here, superscripts $n+1$ and n correspond, respectively, to the t^{n+1} and t^n time levels of a uniformly spaced temporal grid ($t^{n+1} = t^n + \delta t$ where δt is the time step), index i labels cells of a computational grid (with uniform grid spacing δx), half integer indices correspond to cell faces and $\mathcal{U} = (\delta t/\delta x)U$ is the local Courant number.

While the upwind scheme is sign-preserving and has a relatively small phase error, it is plagued by a large implicit diffusion. This is revealed by a simple truncation error analysis[1] of (2.3) which, under a simplifying assumption of constant U and G, results in the advection-diffusion equation

$$\frac{\partial \Psi}{\partial t} + \frac{1}{G}\frac{\partial}{\partial x}(U\Psi) = \frac{1}{G}\frac{\partial}{\partial x}\left(K\frac{\partial \Psi}{\partial x}\right) + \mathcal{O}(\delta t^2, \delta x^2), \tag{2.5}$$

with a diffusion coefficient

$$K = \frac{\delta x^2}{2\delta t}\left(|\mathcal{U}| - \frac{\mathcal{U}^2}{G}\right). \tag{2.6}$$

The diffusive term is the leading-order error of the upwind scheme. While its simple centred-differences compensation leads to the well-known oscillatory one-step Lax-Wendroff scheme, MPDATA ingenuity stems from rewriting this term as a divergence of an advective flux

$$\frac{1}{G}\frac{\partial}{\partial x}\left(K\frac{\partial \Psi}{\partial x}\right) = \frac{1}{G}\frac{\partial}{\partial x}(\overline{U}\Psi), \tag{2.7}$$

where

$$\overline{U} = \frac{\delta x^2}{2\delta t}\left(|\mathcal{U}| - \frac{\mathcal{U}^2}{G}\right)\frac{1}{\Psi}\frac{\partial \Psi}{\partial x} \tag{2.8}$$

is an error-compensating pseudo-velocity. Hence, the error can be compensated by a second iteration of the upwind scheme using the pseudo-velocity as the advective velocity, while preserving the sign of Ψ. Moreover, since the corrective pass is also based on the upwind scheme, the correction can be iterated further. A suitable numerical approximation to the ratio $\frac{1}{\Psi}\frac{\partial \Psi}{\partial x}$ in (2.8) is

$$\frac{1}{\Psi}\frac{\partial \Psi}{\partial x}\bigg|_{i+1/2} \approx \frac{2}{\delta x}\frac{\Psi_{i+1} - \Psi_i}{\Psi_{i+1} + \Psi_i + \epsilon}, \tag{2.9}$$

which, for Ψ of constant sign, ensures the boundness of the pseudo velocity and, consequently, the stability of the scheme (Smolarkiewicz and Margolin, 1998; Smolarkiewicz

[1] Expanding all dependant variables in a Taylor series about (x_i, t^n), dropping i and n as the resulting equation is valid for arbitrary i and n, and converting time derivatives to spatial derivatives using the governing equation. See the next chapter for a more thorough discussion of this procedure in the derivation of the fully third-order scheme.

and Szmelter, 2005; Kühnlein and Smolarkiewicz, 2017). An arbitrary small—e.g.10^{-15} in 64-bit precision for fields with the amplitude of $\mathcal{O}(1)$—constant ϵ is added in the denominator of (2.9) to ensure the validity of the scheme at zeros of Ψ[2].

2.2 Multidimensional MPDATA

One of the main benefits of MPDATA is that it can be used for multidimensional transport in geometrically unsplit fashion, a favourable property for simulating nearly incompressible atmospheric flows. Extending MPDATA to multiple dimensions requires the truncation error analysis of the multidimensional upwind scheme to derive the associated pseudo-velocity (Smolarkiewicz, 1984). The analytical expression for such pseudo-velocity can be compactly written as

$$\overline{\boldsymbol{V}}(\boldsymbol{V},\Psi) = \frac{1}{2}\boldsymbol{\delta x}\odot\uparrow\boldsymbol{V}\uparrow\odot\frac{\nabla\Psi}{\Psi} - \frac{1}{2}\delta t\frac{\boldsymbol{V}}{G}\left[\boldsymbol{V}\cdot\frac{\nabla\Psi}{\Psi}+\nabla\cdot\boldsymbol{V}\right], \tag{2.10}$$

where $(\uparrow\boldsymbol{a}\uparrow)^I := |a^I|$ denotes component-wise absolute value of a vector and $(\boldsymbol{a}\odot\boldsymbol{b})^I := a^I b^I$ is the component-wise (Hadamard) product of two vectors. The standard multidimensional MPDATA proceeds using the iterative form

$$\begin{aligned}\Psi_{\boldsymbol{i}}^{(m)} =& \Psi_{\boldsymbol{i}}^{(m-1)} \\ &- \frac{1}{G_{\boldsymbol{i}}}\sum_{I=1}^{N}\left\{F\left(\Psi_{\boldsymbol{i}}^{(m-1)},\Psi_{\boldsymbol{i}+\boldsymbol{e}^I}^{(m-1)},\mathcal{V}_{\boldsymbol{i}+1/2\,\boldsymbol{e}^I}^{I\ (m)}\right) - F\left(\Psi_{\boldsymbol{i}-\boldsymbol{e}^I}^{(m-1)},\Psi_{\boldsymbol{i}}^{(m-1)},\mathcal{V}_{\boldsymbol{i}-1/2\,\boldsymbol{e}^I}^{I\ (m)}\right)\right\},\end{aligned} \tag{2.11}$$

for $m = 1, M$, where the parenthesised superscripts number the MPDATA iterations. The number of spatial dimensions is N, $\boldsymbol{e}^I$ denotes the unit vector with I indicating the coordinate direction, half integer indices correspond to cell faces. At the start of the algorithm, $\Psi^{(0)} \equiv \Psi^n$, $\mathcal{V}^{I\ (1)} \equiv (\delta t/\delta x^I)(V^I)^{n+1/2}$, where δx^I is the grid spacing in the Ith coordinate direction. The Mth iteration of (2.11) yields the updated solution $\Psi^{n+1} \equiv \Psi^{(M)}$. Note that assumed here is the availability of an estimate for the local Courant number $\mathcal{V}^{I\,(1)}$ at the intermediate time level $t^{n+1/2}$ with at least $\mathcal{O}(\delta t^2)$ accuracy, discussed further in the chapter. The second and subsequent iterations use the nondimensional error-compensating pseudo-velocities

$$\mathcal{V}^{I\ (m)} = \frac{\delta t}{\delta x^I}V^{I\,(m)} = \frac{\delta t}{\delta x^I}\overline{V}^I\left(\boldsymbol{V}^{(m-1)},\Psi^{(m-1)}\right) \qquad \text{for } m>1, \tag{2.12}$$

[2]Implementations with $\epsilon \equiv 0$ are possible but less cost-effective.

based on FD approximations to the analytical expression (2.10). The standard discrete expression is

$$\overline{V}_{i+1/2e^I} = \left[|V^I_{i+1/2e^I}| - \frac{\delta t \left(V^I_{i+1/2e^I}\right)^2}{G_{i+1/2e^I}} \right] \frac{\Psi_{i+e^I} - \Psi_i}{\Psi_{i+e^I} + \Psi_i + \epsilon} - \sum_{J=1, J\neq I}^{M} \frac{\delta t}{2} \frac{V^I_{i+1/2e^I} V^J_{i+1/2e^I}}{G_{i+1/2e^I}} \frac{\Psi_{i+e^I+e^J} + \Psi_{i+e^I} - \Psi_{i+e^I-e^J} - \Psi_{i-e^J}}{\Psi_{i+e^I+e^J} + \Psi_{i+e^I} + \Psi_{i+e^I-e^J} + \Psi_{i-e^J} + \epsilon} - \frac{\delta t}{4} \frac{V^I_{i+1/2e^I}}{G_{i+1/2e^I}} \sum_{J=1}^{M} \left(V^J_{i+e^I+1/2e^J} + V^J_{i+1/2e^J} - V^J_{i+e^I-1/2e^J} - V^J_{i-1/2e^J} \right), \tag{2.13}$$

where $V^J_{i+1/2e^I} = \frac{1}{4}(V^J_{i+e^I+1/2e^J} + V^J_{i+1/2e^J} + V^J_{i+e^I-1/2e^J} + V^J_{i-1/2e^J})$ and $G_{i+1/2e^I} = \frac{1}{2}(G_{i+e^I} + G_i)$. Similarly to the one dimensional case, the adopted discretisation of the term $\frac{\nabla\Psi}{\Psi}$ has the favourable boundness property.

2.3 MPDATA options

The above review presented the basic second-order-accurate MPDATA scheme for transporting fields of constant sign. This section introduces some of the advanced options of the algorithm.

2.3.1 Transporting fields of variable sign

The simplest way of extending MPDATA for transporting fields of variable sign is by exploiting the relationship

$$\frac{1}{\Psi}\frac{\partial \Psi}{\partial x^I} = \frac{1}{|\Psi|}\frac{\partial |\Psi|}{\partial x^I}, \tag{2.14}$$

which amounts to replacing every Ψ by the corresponding absolute value $|\Psi|$ in (2.13). Another approach, introduced in Smolarkiewicz and Clark (1986), is based on the gauge transformation

$$\frac{\partial G(\Psi + c\chi)}{\partial t} + \nabla \cdot [\boldsymbol{V}(\Psi + c\chi)] = 0, \tag{2.15}$$

where c is an arbitrary constant and χ is the fluid density (for elastic systems) or a constant $\chi = 1$ (for anelastic systems). The additional degree of freedom introduced by the transformation can be used to define an asymptotic limit of the MPDATA scheme for $c \to \infty$. This two-pass variant of the scheme, termed "infinite-gauge", is technically achieved by replacing in the second MPDATA iteration the first two arguments of the upwind flux function with unity, substituting every Ψ that enters the denominators of

the pseudo-velocity velocity (2.13) with unity and multiplying the terms independent of Ψ by $\Psi_{\boldsymbol{i}+1/2\boldsymbol{e}^I}$. Since the resulting second-order-accurate scheme is linear and hence oscillatory it is commonly combined with the nonoscillatory option discussed below.

2.3.2 Nonoscillatory option

While sign-preservation is sufficient for a variety of geophysical applications, there are problems where nonoscillatory solutions are needed. In Smolarkiewicz and Grabowski (1990) MPDATA was extended to full monotonicty preservation in the framework of multidimensional FCT (Zalesak, 1979). MPDATA is especially well suited for this because the FCT procedure mixes schemes with similar phase-error properties. The FCT limiting does not depend on the exact form of the pseudo-velocity, hence it is applicable to any variant of MPDATA.

2.3.3 Velocity extrapolation/interpolation

The first iteration of MPDATA requires advective velocities located at the cell faces and taken at the intermediate time level $t^{n+1/2}$. The temporal staggering is necessary to maintain second-order accuracy for time dependant flows. In anelastic fluid solvers based on MPDATA, where the velocity components are part of the prognosed variables, the most common way to obtain $\boldsymbol{V}^{n+1/2}$ is linear extrapolation

$$\boldsymbol{V}^{n+1/2} := \frac{1}{2}(3\boldsymbol{V}^n - \boldsymbol{V}^{n-1}), \tag{2.16}$$

which maintains mass continuity[3].

The prognosed variables are located at the cell centers, to obtain the values at the cell faces linear interpolation

$$V^I_{\boldsymbol{i}+1/2\boldsymbol{e}^I} := \frac{1}{2}(V^I_{\boldsymbol{i}} + V^I_{\boldsymbol{i}+\boldsymbol{e}^I}) \tag{2.17}$$

is commonly used.

2.3.4 Constant coefficients third-order correction

For generalised transport equation with constant coefficients, that is both $\boldsymbol{V}$ and G are constant in (2.1), a third-order accurate variant of MPDATA was derived in Margolin and Smolarkiewicz (1998). The required modification of the psuedo-velocities

[3]The given formula assumes a uniform time step. See Kühnlein et al. (2012) for variable time stepping that also accounts for time-dependent curvilinear coordinates.

of MPDATA are discrete approximations to analytical expressions of the form

$$\begin{aligned}\delta\overline{\mathcal{U}} =& \frac{\delta x^2}{6}\left(\frac{3\mathcal{U}|\mathcal{U}|}{G} - \frac{2\mathcal{U}^3}{G^2} - \mathcal{U}\right)\frac{1}{\Psi}\frac{\partial^2\Psi}{\partial x^2} + \frac{\delta x\delta y\mathcal{V}}{2G}\left(|\mathcal{U}| - \frac{2\mathcal{U}^2}{G}\right)\frac{1}{\Psi}\frac{\partial^2\Psi}{\partial x\partial y} \\ &+ \frac{\delta x\delta z\mathcal{W}}{2G}\left(|\mathcal{U}| - \frac{2\mathcal{U}^2}{G}\right)\frac{1}{\Psi}\frac{\partial^2\Psi}{\partial x\partial z} + \frac{2\delta y\delta z\mathcal{U}\mathcal{V}\mathcal{W}}{3G^2}\frac{1}{\Psi}\frac{\partial^2\Psi}{\partial y\partial z},\end{aligned} \tag{2.18}$$

where modifications of other pseudo-velocity components are obtained by symmetric permutations.

3 Fully third-order MPDATA

In this chapter a third-order accurate MPDATA scheme for spatially and temporally variable flows is developed. The starting point is the derivation of a third-order error-compensating pseudo-velocity based on the leading-order truncation error of standard MPDATA. A unified expression for the resulting pseudo-velocity, including combined effects of various MPDATA options, is presented and discussed. Each term in the expression is labelled and given a clear interpretation based on its origin. Finally, the details of the scheme implementation are presented.

3.1 Derivation of the third-order error-compensating velocity

The derivation of the third-order error-compensating velocity comprises two distinct steps. First, the leading order spatial and temporal truncation error of the second-order MPDATA scheme is derived. Afterwards, the temporal error is converted to a spatial form using the Cauchy-Kowalevski procedure. Importantly, the exact result depends on some of the standard MPDATA options, such as number of iterations or the interpolation/extrapolation procedures discussed in the previous chapter. While the procedure is conceptually simple the calculations can be involving. Hence, to assist hand derivations, an implementation of the procedure in a computer algebra system was created. Both approaches are summarised below, with a step-by-step description of the hand derivation relegated to Appendix A.

3.1.1 Hand derivation

To find the leading-order spatial truncation error of the standard MPDATA every $\Psi_{\boldsymbol{j}}^{(m-1)}$, $\mathcal{V}^{I\ (m)}_{\boldsymbol{j}+1/2\,\boldsymbol{e}^I}$ and $G_{\boldsymbol{j}}$ that appears in the iterative form (2.11) is expanded in a third-order Taylor series in space about a common point $\mathbf{x_i}$. Note that different formulations of the discrete scheme may result in different truncation errors. For example if $V^I_{\boldsymbol{i}+1/2\boldsymbol{e}^I}$ is known with $\mathcal{O}((\delta x^I)^3)$ accuracy then

$$V^I_{\boldsymbol{i}+1/2\boldsymbol{e}^I} = V^I_{\boldsymbol{i}} + \frac{\delta x^I}{2}\,\frac{\partial V^I}{\partial x^I}\bigg|_{\boldsymbol{i}} + \frac{(\delta x^I)^2}{8}\,\frac{\partial^2 V^I}{\partial (x^I)^2}\bigg|_{\boldsymbol{i}} + \mathcal{O}((\delta x^I)^3). \tag{3.1}$$

However, if linear interpolation is used, then

$$V^I_{\boldsymbol{i}+1/2\boldsymbol{e}^I} := \frac{1}{2}(V^I_{\boldsymbol{i}} + V^I_{\boldsymbol{i}+\boldsymbol{e}^I}) = V^I_{\boldsymbol{i}} + \frac{\delta x^I}{2}\frac{\partial V^I}{\partial x^I}\bigg|_{\boldsymbol{i}} + \frac{(\delta x^I)^2}{4}\frac{\partial^2 V^I}{\partial (x^I)^2}\bigg|_{\boldsymbol{i}} + \mathcal{O}((\delta x^I)^3), \quad (3.2)$$

leading to a different coefficient multiplying the second spatial derivative. The resulting system of equations (one for each iteration) is then reduced to a single equation by successively expressing $\Psi^{(m)}_{\boldsymbol{i}}$ in terms of $\Psi^{(m-1)}_{\boldsymbol{i}}$, stopping when Ψ^{n+1} is expressed sorely in terms of Ψ^n. A third-order Taylor series expansion in time of the resulting equation about t^n results in modified equation of the form

$$\frac{\partial \Psi}{\partial t} + \frac{1}{G}\nabla\cdot(\boldsymbol{V}\Psi) = \frac{1}{G}\nabla\cdot(\boldsymbol{T}_F) - \frac{\delta t}{2}\frac{\partial^2 \Psi}{\partial t^2} - \frac{\delta t^2}{6}\frac{\partial^3 \Psi}{\partial t^3} + \mathcal{O}^3(\delta t, \boldsymbol{\delta x}), \quad (3.3)$$

where $\boldsymbol{T}_F$ symbolises the truncation error of the MPDATA fluxes. Notably, the spatial truncation error is in the divergence form as expected for a conservative scheme. Hereafter, $\mathcal{O}^r(\delta t, \boldsymbol{\delta x})$ refers to any terms of order greater or equal to r when considered as a polynomial in the variables δt and $\boldsymbol{\delta x}$. The second-order accuracy of MPDATA is not yet evident, as (3.3) contains a term proportional to δt. This is characteristic of Lax-Wendroff type schemes, which rely on cancellations between spatial and temporal truncation errors. To directly see the second-order accuracy of MPDATA and to obtain the spatial form of the error, the Cauchy-Kowalevski procedure is applied to (3.3). This means successively using (3.3) and its time derivatives to express the truncation error solely in terms of spatial derivatives of the transported scalar. Importantly, for the third-order accuracy, using (3.3) as opposed to (2.1) to perform the conversion is essential (Warming and Hyett, 1974; Margolin and Smolarkiewicz, 1998). The end result can be expressed as follows

$$\frac{\partial \Psi}{\partial t} + \frac{1}{G}\nabla\cdot(\boldsymbol{V}\Psi) = \frac{1}{G}\nabla\cdot(\boldsymbol{T}_S) := \frac{1}{G}\nabla\cdot\left(\overline{\overline{\boldsymbol{V}}}\Psi\right), \quad (3.4)$$

where the $\mathcal{O}^3(\delta t, \boldsymbol{\delta x})$ terms were dropped, $\boldsymbol{T}_S$ symbolises the spatial form of the $\mathcal{O}^2(\delta t, \boldsymbol{\delta x})$ truncation error, and the last equality defines $\overline{\overline{\boldsymbol{V}}}$—the third-order error-compensating velocity. Following the outlined approach, the detailed derivation of the truncation error of the standard MPDATA with two iterations is presented in Appendix A. A unified expression for $\overline{\overline{\boldsymbol{V}}}$, combining the computer algebra extensions presented in the subsequent Section 3.1.2, is shown and discussed in Section 3.2.

3.1.2 Computer algebra implementation

While the procedure presented in the previous subsection is conceptually straightforward, the analytical manipulations can be involving, especially when extensions, such as going beyond two iterations, are considered. To validate and extend the modified equation analysis of MPDATA, the computer algebra system SageMath (The Sage

Developers, 2018)[1] was used to implement the procedure. The implementation uses computer algebra capabilities judiciously to keep the truncation error in the divergence form. The approach is briefly summarised below.

Notwithstanding the iterative nature of MPDATA, the scheme can be formally written as

$$\Psi_{\boldsymbol{i}}^{n+1} = \Psi_{\boldsymbol{i}}^{n} - \frac{1}{G_{\boldsymbol{i}}} \sum_{I=1}^{N} \left[F^{I\ [MP]}_{\boldsymbol{i}+1/2\boldsymbol{e}^I} - F^{I\ [MP]}_{\boldsymbol{i}-1/2\boldsymbol{e}^I} \right], \tag{3.5}$$

where $\boldsymbol{F}^{[MP]}$ is the MPDATA numerical flux, i.e. the sum over all iterations in (2.11). Formally expanding (3.5) to third-order accuracy in time and space leads to (3.3) with

$$\boldsymbol{T}_F = -\frac{\boldsymbol{\delta x}}{\delta t} \odot \left(\boldsymbol{F}^{[MP]} + \frac{\boldsymbol{\delta x} \odot \boldsymbol{\delta x}}{24} \odot \nabla \odot \nabla \odot \boldsymbol{F}^{[MP]} \right) + \boldsymbol{V}\Psi. \tag{3.6}$$

Writing (3.3) as

$$\frac{\partial \Psi}{\partial t} + \frac{1}{G}\nabla \cdot (\boldsymbol{V}\Psi) = \frac{1}{G}\nabla \cdot (\boldsymbol{T}_F) - \frac{\delta t}{2}\frac{\partial}{\partial t}\left(\frac{\partial \Psi}{\partial t}\right) - \frac{\delta t^2}{6}\frac{\partial}{\partial t^2}\left(\frac{\partial \Psi}{\partial t}\right) + \mathcal{O}^3(\delta t, \boldsymbol{\delta x}), \tag{3.7}$$

and noting that

$$\frac{\partial \Psi}{\partial t} = \frac{1}{G}\nabla \cdot (\boldsymbol{T}_F - \boldsymbol{V}\Psi) - \frac{\delta t}{2}\frac{\partial}{\partial t}\left(\frac{\partial \Psi}{\partial t}\right) + \mathcal{O}^2(\delta t, \boldsymbol{\delta x}) = \frac{1}{G}\nabla \cdot (\boldsymbol{T}_F - \boldsymbol{V}\Psi) + \mathcal{O}^1(\delta t, \boldsymbol{\delta x}), \tag{3.8}$$

gives

$$\frac{\partial \Psi}{\partial t} + \frac{1}{G}\nabla \cdot (\boldsymbol{V}\Psi) = \frac{1}{G}\nabla \cdot \left[\boldsymbol{T}_F - \frac{\delta t}{2}\frac{\partial}{\partial t}(\boldsymbol{T}_F - \boldsymbol{V}\Psi) + \frac{\delta t^2}{12}\frac{\partial^2}{\partial t^2}(\boldsymbol{T}_F - \boldsymbol{V}\Psi) \right] + \mathcal{O}^3(\delta t, \boldsymbol{\delta x}). \tag{3.9}$$

Equation (3.9) is the starting point for the automated Cauchy-Kowalevski procedure, which is only applied to the terms under the divergence operator on the rhs of (3.9), thus keeping the result in the divergence form.

[1] https://www.sagemath.org

3.2 Third-order error-compensating velocity

The explicit expression for the third-order error-compensating velocity $\overline{\overline{\boldsymbol{V}}}$ is

$$\begin{aligned}\overline{\overline{\boldsymbol{V}}}(\boldsymbol{V},\overline{\boldsymbol{V}},\Psi) = &\underbrace{-\frac{\boldsymbol{\delta x}\odot\boldsymbol{\delta x}}{24}\odot\left[4\boldsymbol{V}\odot\frac{1}{\Psi}\nabla\odot\nabla\Psi+2\frac{\nabla\Psi}{\Psi}\odot\nabla\odot\boldsymbol{V}+\alpha\nabla\odot\nabla\odot\boldsymbol{V}\right]}_{A}\\
&\underbrace{+\beta_M\frac{\boldsymbol{\delta x}}{2}\odot\left\uparrow\overline{\boldsymbol{V}}\right\uparrow\odot\frac{\nabla\Psi}{\Psi}}_{B}+\underbrace{\frac{\delta t}{2}\boldsymbol{\delta x}\odot\uparrow\boldsymbol{V}\uparrow\odot\frac{1}{\Psi}\nabla\left[\frac{1}{G}\nabla\cdot(\boldsymbol{V}\Psi)\right]}_{C}\\
&\underbrace{-\frac{\delta t^2}{3}\frac{\boldsymbol{V}}{G\Psi}\nabla\cdot\left[\frac{\boldsymbol{V}}{G}\nabla\cdot(\boldsymbol{V}\Psi)\right]}_{D}\\
&\underbrace{+\frac{\delta t^2}{24}\left[\gamma\frac{\partial^2\boldsymbol{V}}{\partial t^2}+\frac{2\boldsymbol{V}}{G\Psi}\nabla\cdot\left(\frac{\partial\boldsymbol{V}}{\partial t}\Psi\right)-\frac{2}{G\Psi}\frac{\partial\boldsymbol{V}}{\partial t}\nabla\cdot(\boldsymbol{V}\Psi)\right]}_{E},\end{aligned}\tag{3.10}$$

where α, β_M and γ are parameters that result from different MPDATA formulations.

All terms on the rhs of (3.10) originate from a source of third-order error in the basic algorithm and has a clear interpretation; for the subsequent discussion they are labelled with letters A to E. The first two terms A and B both originate from upwind differencing, with A corresponding to the third-order error of the first upwind pass, and B related to the upwinding based on the pseudo-velocity in the second pass. Noteworthy, the term B is $\mathcal{O}^2(\delta t,\boldsymbol{\delta x})$ as $\overline{\boldsymbol{V}}$ is composed of terms proportional to $\boldsymbol{\delta x}$ and δt. The term C is a result of the iterative nature of MPDATA; specifically, it comes from using the first-order accurate upwind solution in calculating gradients of Ψ that enter the pseudo-velocity formula (2.10). The last two terms D and E are both related to the forward-in-time differencing errors. This terms differ, because D derives only from the temporal variations of Ψ, whereas E includes contributions from the time-varying velocity field. In the case of stationary flow the term E vanishes identically.

The parameters α, β_M and γ on the rhs of (3.10) combine three different MPDATA options into a common formula. Within the limits of the third-order accurate analysis, the only effect of increasing the number of MPDATA passes beyond two is the cancellation of the B term. Consequently, β_M is equal to 1 if $M = 2$ and 0 otherwise. The other two parameters account for the effects of the standard interpolation/extrapolation procedures for the velocity. The parameter α is equal to 4 when the standard linear interpolation $V^I_{\boldsymbol{i}+1/2\boldsymbol{e}^I} = \frac{1}{2}(V^I_{\boldsymbol{i}} + V^I_{\boldsymbol{i}+\boldsymbol{e}^I})$ is used, and 1 if $V^I_{\boldsymbol{i}+1/2\boldsymbol{e}^I}$ is known to $\mathcal{O}(\boldsymbol{\delta x}^3)$. In principle a higher-order interpolation could be used, however, it is usually more convenient to account for this error directly in the third-order error-compensating velocity. Similarly, the parameter γ is related to the linear extrapolation $\boldsymbol{V}^{n+1/2} = \frac{1}{2}(3\boldsymbol{V}^n - \boldsymbol{V}^{n-1})$. The error of this estimate can also be directly incorporated

into the third-order error-compensating velocity by choosing $\gamma = 10$. Otherwise, if $\boldsymbol{V}^{n+1/2}$ is at least $\mathcal{O}(\delta t^3)$ accurate, $\gamma = 1$. The meaning and values of α, β_M and γ are collected in Table 3.1.

Tabela 3.1
Summary of various options in MPDATA and the corresponding values of the parameters α, β_M and γ appearing in (3.10).

Condition	Parameter	Value
$V^I_{\boldsymbol{i}+1/2\boldsymbol{e}^I}$ is at least $\mathcal{O}(\boldsymbol{\delta x}^3)$ accurate	α	1
$V^I_{\boldsymbol{i}+1/2\boldsymbol{e}^I} = \frac{1}{2}(V^I_{\boldsymbol{i}} + V^I_{\boldsymbol{i}+\boldsymbol{e}^I})$	α	4
$M = 2$	β_M	1
$M > 2$ or infinite-gauge	β_M	0
$\boldsymbol{V}^{n+1/2}$ is at least $\mathcal{O}(\delta t^3)$ accurate	γ	1
$\boldsymbol{V}^{n+1/2} = \frac{1}{2}(3\boldsymbol{V}^n - \boldsymbol{V}^{n-1})$	γ	10

3.3 Construction and implementation of the fully third-order accurate MPDATA

Here, a third-order accurate MPDATA is constructed based on the expression for the third-order error-compensating velocity. As in the standard MPDATA, the general idea is to subtract an estimate of the third-order error by using $\overline{\overline{\boldsymbol{V}}}$ in an upwind iteration. In the simplest way, it can be done in just two iterations of the form (2.11), by replacing the nondimensional pseudo-velocity in the second iteration (2.12) with the sum of the standard MPDATA pseudo-velocity and the third-order error-compensating pseudo-velocity

$$\mathcal{V}^{I\ (2)} = \frac{\delta t}{\delta x^I}\left[\overline{V}^I\left(\boldsymbol{V}^{(1)}, \Psi^{(1)}\right) + \overline{\overline{V}}^I\left(\boldsymbol{V}^{(1)}, \overline{\boldsymbol{V}}(\boldsymbol{V}^{(1)}, \Psi^{(1)}), \Psi^{(1)}\right)\right]. \tag{3.11}$$

Performing only two iterations is computationally efficient and can benefit parallel distributed-memory communication. However, it is worth pointing out other possibilities, potentially admitting larger time steps δt,[2] such as first proceeding with all of the standard MPDATA iterations and then applying an extra upwind pass based solely on $\overline{\overline{\boldsymbol{V}}}$.

[2]Implementations summing pseudo-velocities of corrective iterations generally have more restrictive Courant-number condition sufficient for the linear stability; see §5.5 in Smolarkiewicz (1984) and §6.1 in Margolin and Smolarkiewicz (1998) for discussions.

The discrete formulation of $\overline{\overline{\boldsymbol{V}}}$ completes the definition of the fully third-order accurate scheme. Following the decomposition in (3.10), $\overline{\overline{V}}^I_{i+1/2e^I} = A_d + B_d + C_d + D_d + E_d$, where

$$\begin{aligned} A_d =& -\frac{1}{3}V^I_{i+1/2e^I}\frac{|\Psi_{i+2e^I}| - |\Psi_{i+e^I}| - |\Psi_i| + |\Psi_{i-e^I}|}{|\Psi_{i+2e^I}| + |\Psi_{i+e^I}| + |\Psi_i| + |\Psi_{i-e^I}| + \epsilon} \\ &- \frac{1}{12}\left(V^I_{i+3/2e^I} - V^I_{i-1/2e^I}\right)\frac{|\Psi_{i+e^I}| - |\Psi_i|}{|\Psi_{i+e^I}| + |\Psi_i| + \epsilon} \\ &- \frac{\alpha}{24}\left(V^I_{i+3/2e^I} + V^I_{i-1/2e^I} - 2V^I_{i+1/2e^I}\right), \end{aligned} \tag{3.12}$$

$$B_d = \beta_M|\overline{V}^I_{i+1/2e^I}|\frac{|\Psi_{i+e^I}| - |\Psi_i|}{|\Psi_{i+e^I}| + |\Psi_i| + \epsilon}, \tag{3.13}$$

$$C_d = \frac{\delta t}{2}\frac{|V^I_{i+1/2e^I}|}{\langle|\Psi|\rangle_C + \epsilon}\left\{\frac{[\nabla\cdot(\boldsymbol{V}|\Psi|)]_{i+e^I}}{G_{i+e^I}} - \frac{[\nabla\cdot(\boldsymbol{V}|\Psi|)]_i}{G_i}\right\}, \tag{3.14}$$

$$\begin{aligned} D_d =& -\frac{\delta t^2}{3}\frac{V^I_{i+1/2e^I}}{G_{i+1/2e^I}(\langle|\Psi|\rangle_D + \epsilon)}\times \\ &\sum_{J=1}^{N}\frac{1}{\delta x^J}\left\{\frac{[\nabla\cdot(\boldsymbol{V}|\Psi|)]_{i+1/2e^I+1/2e^J}}{G_{i+1/2e^I+1/2e^J}} - \frac{[\nabla\cdot(\boldsymbol{V}|\Psi|)]_{i+1/2e^I-1/2e^J}}{G_{i+1/2e^I-1/2e^J}}\right\}, \end{aligned} \tag{3.15}$$

$$\begin{aligned} E_d =& \frac{\delta t^2\gamma}{24}\left(\frac{\partial^2 V^I}{\partial t^2}\right)_{i+1/2e^I} + \frac{\delta t^2 V^I_{i+1/2e^I}}{12G_{i+1/2e^I}(\langle|\Psi|\rangle_E + \epsilon)}\left[\nabla\cdot\left(\frac{\partial\boldsymbol{V}}{\partial t}|\Psi|\right)\right]_{i+1/2e^I} \\ &- \frac{\delta t^2}{12G_{i+1/2e^I}(\langle|\Psi|\rangle_E + \epsilon)}\left(\frac{\partial V^I}{\partial t}\right)_{i+1/2e^I}[\nabla\cdot(\boldsymbol{V}|\Psi|)]_{i+1/2e^I}. \end{aligned} \tag{3.16}$$

Like in all previous MPDATA formulations, normalisation of the truncation error expressions with $\sim\Psi$ is performed in a way that ensures boundedness of the error-compensating pseudo-velocities, and thus the stability of the scheme. Specifically, the normalisation is constructed as an average over all discrete Ψ's that enter the discretisation of the term that this factor is multiplying. This is written explicitly in (3.12)-(3.13), and symbolically as $\langle|\Psi|\rangle_C$, $\langle|\Psi|\rangle_D$ and $\langle|\Psi|\rangle_E$ in (3.14)-(3.16). Note that (3.12)-(3.16) is already extended for transport of fields with variable sign in the standard way, by replacing every Ψ with the corresponding absolute value $|\Psi|$. Similarly, a small constant ϵ added in the normalisations in (3.12)-(3.16) ensures the validity of the scheme when $\langle|\Psi|\rangle_{\ldots} = 0$.

The divergence of a product of an arbitrary vector field $\boldsymbol{\omega}$ with a scalar field ϕ is formulated as

$$[\nabla\cdot(\boldsymbol{\omega}\phi)]_i = \sum_{I=1}^{N}\frac{1}{\delta x^I}\left(\omega^I_{i+1/2e^I}\phi_{i+1/2e^I} - \omega^I_{i-1/2e^I}\phi_{i-1/2e^I}\right). \tag{3.17}$$

Whenever the values of scalar or vector fields are needed at points where they are not

located, a suitable average based on the minimal number of points is used, for example $\phi_{\boldsymbol{i}+1/2\boldsymbol{e}^I} = \frac{1}{2}(\phi_{\boldsymbol{i}+\boldsymbol{e}^I} + \phi_{\boldsymbol{i}})$ for a scalar field and $\boldsymbol{\omega}_{\boldsymbol{i}} = \frac{1}{2}(\boldsymbol{\omega}_{\boldsymbol{i}+1/2\boldsymbol{e}^I} + \boldsymbol{\omega}_{\boldsymbol{i}-1/2\boldsymbol{e}^I})$ for a vector field. Especially in the context of fluid solvers, the expressions for the first and second time derivative of velocity in (3.16) have to be known only to $\mathcal{O}(\delta t)$ in order to ensure the third-order accuracy of the scheme. Consequently, simple backward differentiation formulae can be used to obtain them.

The enhancements to the standard MPDATA algorithm discussed in the previous chapter, such as the nonoscillatory option and the infinite-gauge, carry over to the proposed scheme. In addition to the standard alterations, the infinite-gauge variant sets the value of the parameter $\beta_M = 0$.

4 Open implementation of the fully third-order MPDATA

The fully-third order MPDATA scheme was implemented in an open-source library of MPDATA-based solvers, *libmpdata++* (Jaruga et al., 2015). This chapter presents highlights of the library, particularly stressing the design choices allowing easy, efficient, and maintainable implementation of the new scheme.

4.1 Library organisation

Following the principle of separation of concerns (Hürsch and Lopes, 1995), the library is separated into four components, each handling a separate aspect of the solution procedure. The four components are

- Numerical solvers,
- Boundary conditions,
- Concurrency handlers,
- Output mechanisms.

The separation benefits code maintainability and extensibility, as every component can be developed independently from the others. A diagram showing library organisation can be seen in Figure 4.1.

4.1.1 Numerical solvers

The numerical solvers available in *libmpdata++* are organised in a hierarchical fashion. This organisation is not only conceptual, but actually realised at the code level. Technically, this is achieved by using the inheritance feature of object-oriented programming. More advanced solvers build upon the more basic, and each solver can be used in a stand-alone fashion. This approach has two main benefits. Firstly, there is no code duplication, so each feature added to a base solver is automatically propagated to the solvers inheriting from it. Secondly, a problem-specific feature-minimal solver can be chosen, while more advanced but unnecessary components will not be even compiled.

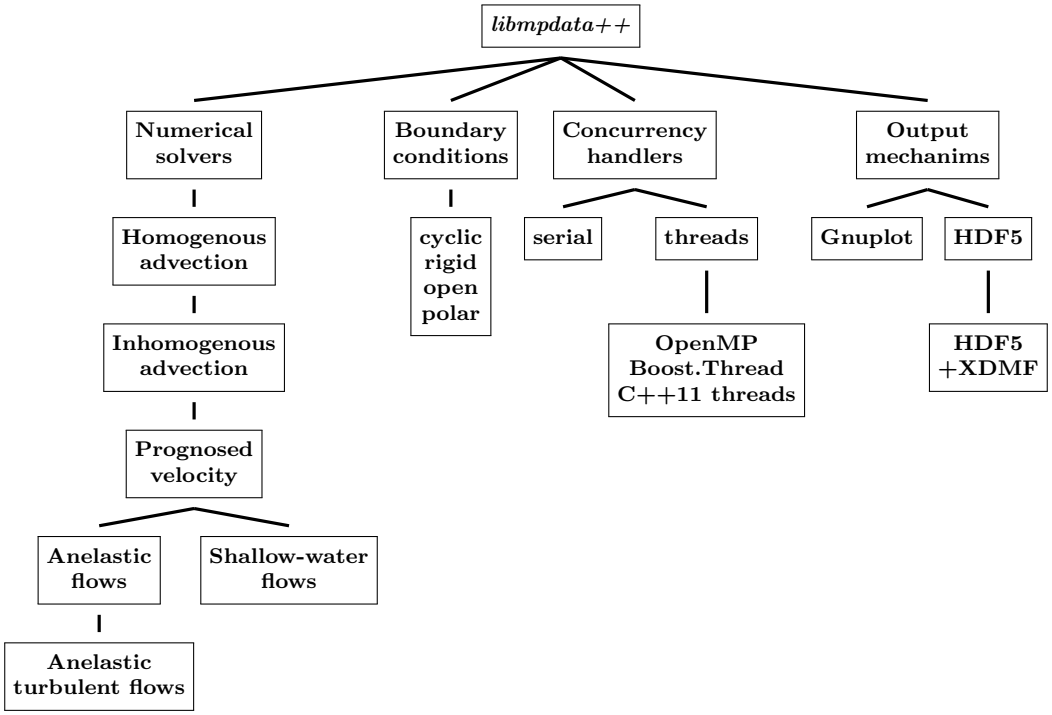

Fig. 4.1. Organisation of the *libmpdata++* library.

For example, for a pure transport problem there is no need to compile the code for handling source terms. This benefits library testability, as basic solvers can be first tested in isolation from more advanced aspects. Then, only the advanced features have to be tested, as the basic ones have already been verified. Moreover, there are obvious performance benefits, since only the necessary operations are executed.

The most basic *libmpdata++* solver handles homogeneous advection problems in one, two, or three dimensions. A direct extension of this solver performs advection with temporal integration of arbitrary source terms. Both of the above solvers require a kinematic setup, with a prescribed velocity field. To solve problems where the velocity field is one of the dependent variables, the prognosed velocity solver is available. This solver can be used to model many purely hyperbolic problems in an explicit way, such as the shallow water equations. In fact, as an example extension, a shallow water solver is already included with *libmpdata++*. The shallow water solver was applied in Jarecka et al. (2015) to compare originally-derived analytical solutions of a spreading drop of water with direct numerical simulations. A more complex extension of the prognosed velocity solver handles the anelastic fluid equations, commonly used in small-scale atmospheric modelling. The anelastic constraint is enforced by the pressure-projection technique (Chorin, 1967), requiring the solution of an elliptic problem. While there are a few elliptic solvers implemented in *libmpdata++*, the most advanced (and the library default) is a bespoke generalised conjugate residual solver (See Smolarkiewicz and Margolin (2000); Smolarkiewicz and Szmelter (2011) for a discussion). Finally,

libmpdata++ provides a solver for anelastic flows with explicit subgrid-scale modelling capability. Currently, the Smagorinsky turbulence model is implemented, and the solver can also be used to solve the Navier-Stokes equations with constant viscosity, in the spirit of direct numerical simulations.

4.1.2 Boundary conditions

libmpdata++ implements three commonly used types of boundary conditions: periodic, rigid-lid, and open. Additionally, special "polar" conditions for simulations on the sphere are available; they are formulated based on the principles of differential geometry (Szmelter and Smolarkiewicz, 2010). Periodic, rigid, and open boundaries can be chosen independently in each dimension. This enables a wide range of setups in three dimensions. Triply-periodic idealised studies of turbulence, horizontally periodic atmospheric LES with impermeable ground and a capping inversion, or a flow in an open-ended channel can all be realised.

4.1.3 Concurrency handlers

Currently, *libmpdata++* allows serial and shared-memory parallel execution using threads. Threads concurrency handler is an abstract interface that can be implemented using different concrete backends. For example, *libmpdata++* includes implementations using the OpenMP library, the Boost.Thread library, or the standard C++11 threads. This benefit performance portability, since the best performing backend can be chosen for any platform. Moreover, extending the available backends with vendor-provided optimised implementations is possible.

4.1.4 Output mechanisms

There are three provided mechanisms for outputting information from *libmpdata++*. The most basic relies on a C++ interface to the gnuplot plotting software. It allows constructing plots on the fly, without having to store the output data. This is preferable for simple examples, especially for teaching purposes. However, for most simulations output data needs to be stored. For that purpose, *libmpdata++* provides data output in the HDF5 format. Optionally, the HDF5 files can be extended with XDMF annotations, understood by a professional visualisation software, such as ParaView. The plain HDF5 output is still useful for one-dimensional simulations, that usually do not benefit from XDMF annotations.

4.2 Library design

Developers of scientific software usually also are its end users. Spending time to make scientific software easy to use can be offset by the productivity gains, especially when

the software is used over a long period of time. This is typically the case for modelling codes, which require considerable upfront effort and implementations of specialised numerical algorithms. The software also has to be maintained for many years, and on many computer systems. To enable productivity and ensure long-term maintainability, *libmpdata++* was developed in accordance with best practices for scientific software development (Wilson et al., 2014). After conducting research into object-oriented implementations of MPDATA in different programming languages (Arabas et al., 2014), the C++ programming language was chosen to implement the library. C++ was chosen, because it is a high-level language, that is also high-performance capable and has a wealth of mature libraries for many purposes.

In the course of library development, the following best practices were particularly stressed

- keeping the code concise and readable,
- maximising code reuse,
- writing the code at the highest level of abstraction that allows reasonable performance,
- having a central public repository where the most recent version of the library resides,
- using a version control system,
- having a suite of tests,
- automatic testing after every merged change.

4.3 Code availability

Many problems of scientific computing, in particular the problem of research reproducibility, are linked to a typically closed source status of the underlying software (Merali, 2010). There is a growing sentiment that for truly reproducible research the software has to be made open (Morin et al., 2012; Ince et al., 2012), and maybe even peer-reviewed. The developers of *libmpdata++* fully embrace this principles. The library is freely available at the project repository[1] and is released under the GPLv3 licence[2]. Not only is the source code released, but the whole history of modifications to the code is available, and versions used for simulations in specific papers are tagged. When developing the library, it is our policy that every major change is peer-reviewed by a developer other than the author of the changes. The library documentation and users

[1] https://github.com/igfuw/libmpdataxx
[2] https://www.gnu.org/licenses/gpl-3.0.html

guide are available in Jaruga et al. (2015), alongside a presentation of selected test results.

4.4 Implementing fully third-order MPDATA in *libmpdata++*

The design of *libmpdata++* enabled fairly easy implementation of the fully third-order accurate MPDATA scheme. The scheme was implemented and tested gradually, starting from homogeneous advection in one dimension, and ending with a three-dimensional implementation in the prognosed velocity framework. Template programming constructs available in C++ allowed concise code representation of numerical expressions, minimising the possibility of errors. For example, only one component of pseudo-velocity had to be hand-written, while other components were generated automatically without performance penalty. Most of the implementation code was localised in numerical solvers, and did not touch other concerns, such as parallelisation and output.

The initial work quickly paid off by allowing the use of the full range of library features with the fully third-order accurate scheme. The library extensive test suite was used to check the implementation. Furthermore, the scheme could be immediately tested on a variety of already established setups. Efficient parallelisation allowed to perform a large number of simulations quickly, which was essential for a detailed study of the scheme benefits. The homogeneous advection solver was used to perform simulations presented in the next chapter, while later chapters show results obtained by employing the anelastic turbulent flows solver.

5 Numerical advection tests

Herein the newly developed fully third-order accurate MPDATA is verified and its merits are assessed compared to the established variants of the scheme. Three test problems are considered, solely in the context of the homogeneous transport equation (2.1), for which sufficiently smooth genuine solutions are known, at least in selected time instants, thereby enabling rigorous accuracy analysis. The first test problem uses a bespoke 3D solution with a stationary Jacobian and a non-stationary generalised flow field, manufactured to verify the correctness of the theoretical development and its numerical implementation (Roache, 2002). The remaining two problems employ established benchmarks (Nair and Jablonowski, 2008; Lauritzen et al., 2012), designed to typify difficulties encountered in a long range tracer advection at the heart of atmospheric chemistry-transport models. Such models are of the utmost importance to monitoring, forecasting and controlling air pollution across scales from micrometeorology to climate; see Pudykiewicz (1989); Hundsdorfer et al. (1995); Frohn et al. (2002); Carmichael et al. (2008); White III and Dongarra (2011); Santillana et al. (2016) for a sample of representative works that address relevant computational issues over the three decades. Both benchmarks idealise two-dimensional tracer transport on the sphere in rotating deformational flows. The first benchmark addresses a cross-polar transport in a velocity field composed of two vortices advected over the poles; whereas, the second focuses on tracer correlations in a reversible deformational flow that leads to tracer filamentation and its reversal—the latter phase being important to source detection of, e.g., nuclear testing (Pudykiewicz, 1998).

5.1 Common setup

In all three advection tests the fully third-order accurate scheme is compared with MPDATA using the constant-velocity third-order correction from Margolin and Smolarkiewicz (1998). For tracer transport on the sphere results using the nonoscillatory infinite-gauge variant of second-order accurate MPDATA are provided as a reference. In those examples, the nonoscillatory infinite-gauge variant of the fully third-order accurate scheme is also examined to see how well the new advancement combines with the previous developments. Table 5.1 lists all the schemes used in the thesis. The

numerical solution error was measured in the standard ℓ_2 norm

$$\ell_2 = \sqrt{\frac{\sum_i G_i(\Psi_i - \Psi_i^e)^2}{\sum_i G_i(\Psi_i^e)^2}} \tag{5.1}$$

where Ψ_i^e is the exact solution evaluated at the point $\boldsymbol{x}_i$.

As every test considered here uses a prescribed time-dependent flow field, the velocities at the intermediate time level $t^{n+1/2}$ were calculated directly from the analytical expressions. For the manufactured solution and the reversing deformational flow the velocities were evaluated directly at the cell faces, whereas in the moving vortices test the velocity was first calculated at the grid points and then interpolated (cf. the second row in Table 3.1). Similarly, the time derivatives of velocity, needed in (3.16), were calculated based on the analytical formulae for the manufactured solution and the reversing deformational flow but based on second-order centred finite-differences for the moving vortices.

Tabela 5.1
Summary and labels of the various MPDATA formulations utilised in the simulations presented in Chapter 5, Chapter 6 and Chapter 7.

Label	Scheme
Mp2	fully second-order-accurate MPDATA
Mp3	fully third-order-accurate MPDATA
Mp3cc	third-order-accurate constant-coefficient MPDATA
Mg2No	nonoscillatory infinite-gauge variant of Mp2
Mg3No	nonoscillatory infinite-gauge variant of Mp3
Mg3ccNo	nonoscillatory infinite-gauge variant of Mp3cc

5.2 Manufactured solution in 3D

Using the method of manufactured solutions (Roache, 2002) the following analytical solution of the transport equation (2.1) was constructed

$$\Psi(t, \boldsymbol{x}) = (2 + \sin t \sin x)(2 + \sin t \sin y)(2 + \sin t \sin z) \ , \tag{5.2}$$

with the corresponding coefficients

$$G(\boldsymbol{x}) = e^{\cos x + \cos y + \cos z} \ , \tag{5.3}$$

$$V^I(t, \boldsymbol{x}) = \frac{G \cos t}{2 + \sin t \sin x^I} \ . \tag{5.4}$$

The solution Ψ can be interpreted as a fluid density that obeys the continuity equation formulated in curvilinear coordinates with the Jacobian G. Note that the flow field

contains regions of strong convergence and divergence (the ratio of the divergence reciprocal to the advective time scale is ~ 0.1 near the divergence extrema), consequently the uniform initial condition $\Psi(0, \boldsymbol{x}) = 8$ gets shaped into a sinusoidal pattern.

The generalised transport equation (2.1) was solved in a triply periodic domain $[0, 2\pi] \times [0, 2\pi] \times [0, 2\pi]$ discretised on a $N \times N \times N$ regular Cartesian grid. For the convergence study a range of values $N = 9, 17, 33, 65, 129$ was chosen. The time step was continuously adapted such that the maximum Courant number did not exceed 0.5. The solution error was calculated at the final time $t = 1$, chosen to prevent the possibility of error cancellations due to the flow symmetries.

Two sets of simulations were performed, one using the proposed fully third-order accurate MPDATA (Mp3), and second using the established MPDATA that is third-order accurate for constant flows (Mp3cc). Convergence of the error measure under the grid refinement is shown in Figure 5.1. Results confirm the third-order convergence of the Mp3 scheme, while the convergence of the Mp3cc scheme reduces to second-order due to the variability of the flow.

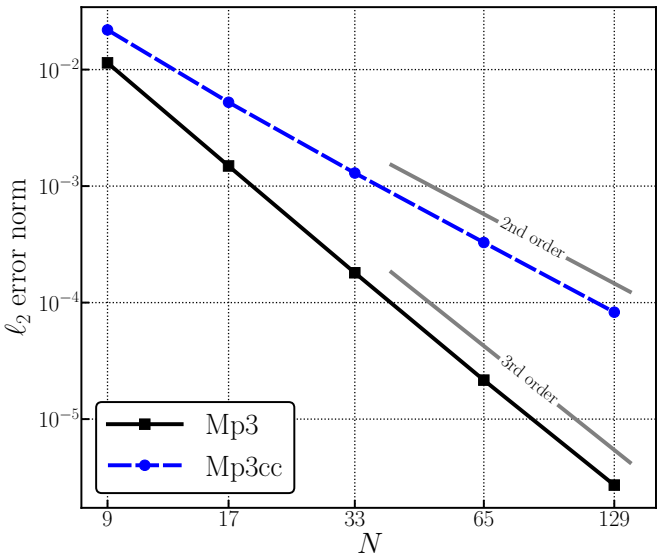

Fig. 5.1. Numerical convergence to the manufactured solution in the ℓ_2 error norm at time $t = 1$.

5.3 Moving vortices

To assess the accuracy of the fully third-order accurate scheme for tracer transport on the sphere a two-dimensional test case was adopted from Nair and Jablonowski (2008). It specifies an initial distribution of a tracer field together with a non-divergent, variable in time and space, deformational flow field such that the analytical solution of (2.1) at any given moment is readily available. The flow field is composed of two vortices, which are always located on the opposite sides of the sphere and embedded

in a background solid-body rotation. Here, the rotation angle of the background flow was set to $\pi/2$, corresponding to the cross-polar flow. All other parameters of the test case were set following the numerical experiments in Nair and Jablonowski (2008). Initially, the centre of one of the vortices was located at $(3\pi/2, 0)$ in longitude-latitude coordinates. Consequently, the initial position of the second vortex was $(\pi/2, 0)$. One full rotation of the vortices over the poles takes 12 days. Figure 5.2a and Figure 5.2b depict the initial condition of the tracer field and its exact distribution after 12 days, respectively.

The numerical solution was computed on a regular longitude-latitude grid with $(2N + 1) \times N$ points, corresponding to uniform $\delta\lambda = \delta\theta = \pi/N$ grid increments. Simulations were run with $N = 24, 48, 96, 192, 384, 768$. Differencing in the vicinity of the poles follows the principles of differential geometry applied to the longitude-latitude coordinate system, see Szmelter and Smolarkiewicz (2010) for a discussion. As in the preceding example the time step was continuously adapted to keep the maximum Courant number less than a prescribed value, here equal to 1. The simulation time of 12 days corresponds to one full rotation of the vortices over the poles. Here, selected schemes of Table 5.1 are compared. Two of them are the same as in the preceding example—the novel Mp3 scheme and the established Mp3cc scheme. Moreover, the Mg3No scheme combines the novel third-order infinite-gauge with the nonoscillatory option. Simulations using the standard nonoscillatory infinite-gauge MPDATA (Mg2No) serve as a reference to evaluate accuracy of the third-order schemes.

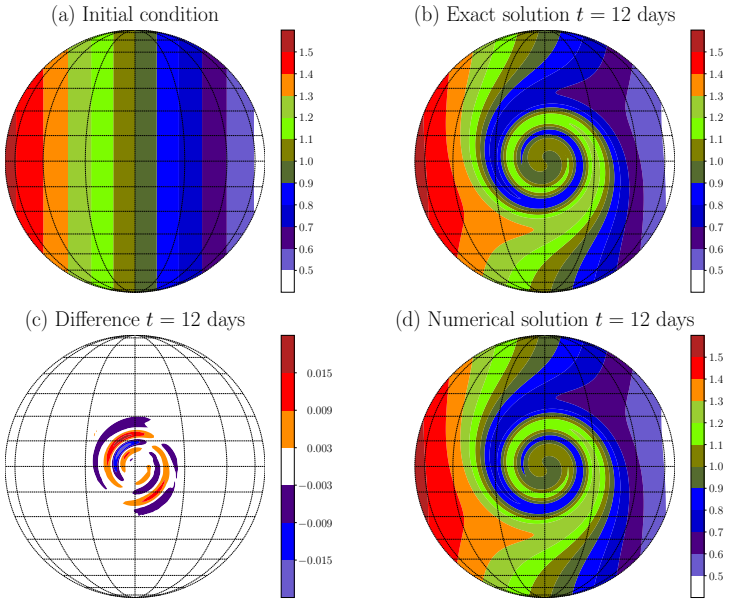

Fig. 5.2. The initial condition (a) together with the analytical solution (b), the difference between the numerical and the analytical solution (c) and the numerical solution (d) after one rotation of the vortices over the poles for the moving vortices test case. The numerical solution was obtained using the Mp3 scheme on a grid with $N = 192$, see Section 5.3 for details.

Convergence in the ℓ_2 error measure with increasing resolution is shown in Figure 5.3. In the range of simulated N the proposed Mp3 scheme converges the fastest at a rate slightly higher than third. In contrast, the Mp3cc scheme does not sustain a third-order rate and reduces to second-order convergence. Enforcing monotonicity in the third-order accurate Mg3No leads to a significant loss of accuracy and basically second-order convergence. The reference Mg2No shows the largest errors and second-order convergence achieved only over the finest grids. Even though three of the four schemes end up converging at a second-order rate, there are marked differences between their accuracy. On the finest grid $N = 768$, the ℓ_2 error norms span almost two orders of magnitude between the various schemes.

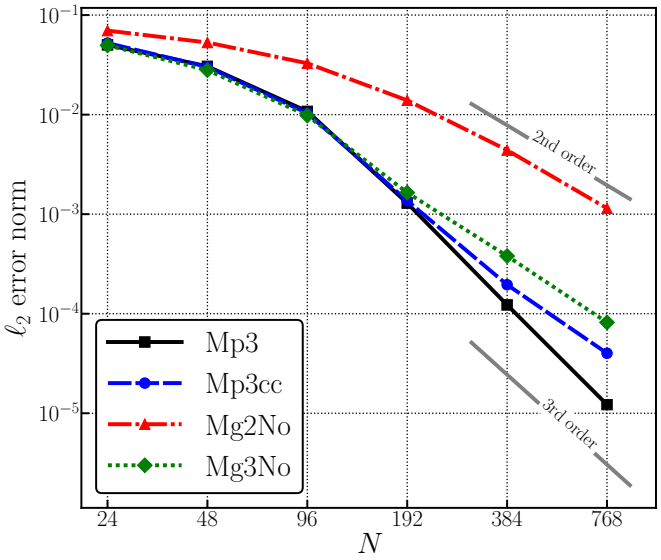

Fig. 5.3. Numerical convergence in the ℓ_2 error norm for the moving vortices test case. The error was evaluated after one rotation of the vortices over the poles.

Table 5.2 lists runtimes of the MPDATA schemes relative to the upwind scheme, based on the $N = 192$ simulations.

Tabela 5.2
Runtimes of the MPDATA schemes relative to the upwind scheme, based on the moving vortices test case. See Section 5.3 for details.

Upwind	Mp2	Mg2No	Mp3cc	Mp3	Mg3No
1.0	3.6	5.9	9.5	10.3	12.6

In addition, the sign-preserving second-order accurate MPDATA scheme (Mp2) is also included for reference. The relative runtimes for Mp2 and Mp3 are ~ 3.6 and ~ 10.3, respectively, i.e. roughly a cost factor of ~ 3 to increase the order by one (up to three). The relative runtimes for the two monotone MPDATA schemes are ~ 5.9 and ~ 12.6, showing the significantly smaller cost increase when going from second- to

third-order than first- to second-order. Importantly, the fully third-order accurate Mp3 scheme is only slightly more expensive than the constant-coefficients variant Mp3cc.

5.4 Reversing deformational flow

In Lauritzen et al. (2012), the authors introduced a test suite for a two-dimensional transport on the sphere using various prescribed time-dependent deformational flow fields. Results of the test suite for a variety of state-of-the-art schemes were collected in Lauritzen et al. (2014). Here, selected diagnostics from this test suite are evaluated for the schemes tested in Section 5.3.

The setup specifies four different initial conditions for the tracer field, each composed of two distributions in the same shape centred at $(\pi/2, 0)$ and $(3\pi/2, 0)$, respectively. The four different shapes are Gaussian hill, cosine bell, slotted cylinder and 'correlated' cosine bell. Two wind fields, one non-divergent and one divergent, were prescribed in the test suite. Here, only diagnostics based on the non-divergent wind field are considered. As in the previous example, the flow field is composed of a deformational part and the solid-body rotation part. The solid-body rotation is purely in the zonal direction. Contrary to the previous example, the deformational part of the flow has a temporal dependence that leads to the flow reversal halfway through the rotation. Hence, after the full rotation, the initial conditions should be recovered. For the detailed specification of the setup in terms of analytical formulae the reader is referred to Lauritzen et al. (2012).

As in the preceding example, a regular longitude-latitude grid with $(2N + 1) \times N$ points was used. Simulations were performed with $N = 60, 120, 240, 480, 960$ corresponding to $\delta\lambda = \delta\theta$ between 3° and 0.1875°. Again, a variable time step was employed with the maximum Courant number kept just under 0.8. The total time of each simulation corresponded to one full rotation.

Figure 5.4 shows the numerical solution for each initial condition, midway through the simulation, obtained with the Mg3No scheme using a $\delta\lambda = 1.5^\circ$ grid interval. No oscillations can be seen, even for the discontinuous slotted cylinders initial conditions (Figure 5.4c). More quantitatively, normalised deviations from the initial extrema $(\min \Psi^n - \min \Psi^0)/\max \Psi^0 = 0$ and $(\max \Psi^n - \max \Psi^0)/\max \Psi^0 = -0.001$ for the slotted cylinders at the time of the maximal deformation. This shows the effective combination of the developed third-order scheme with the nonoscillatory option of MPDATA. Overall, the filamentary structure of the solutions at the time of the maximal deformation seems to be well captured.

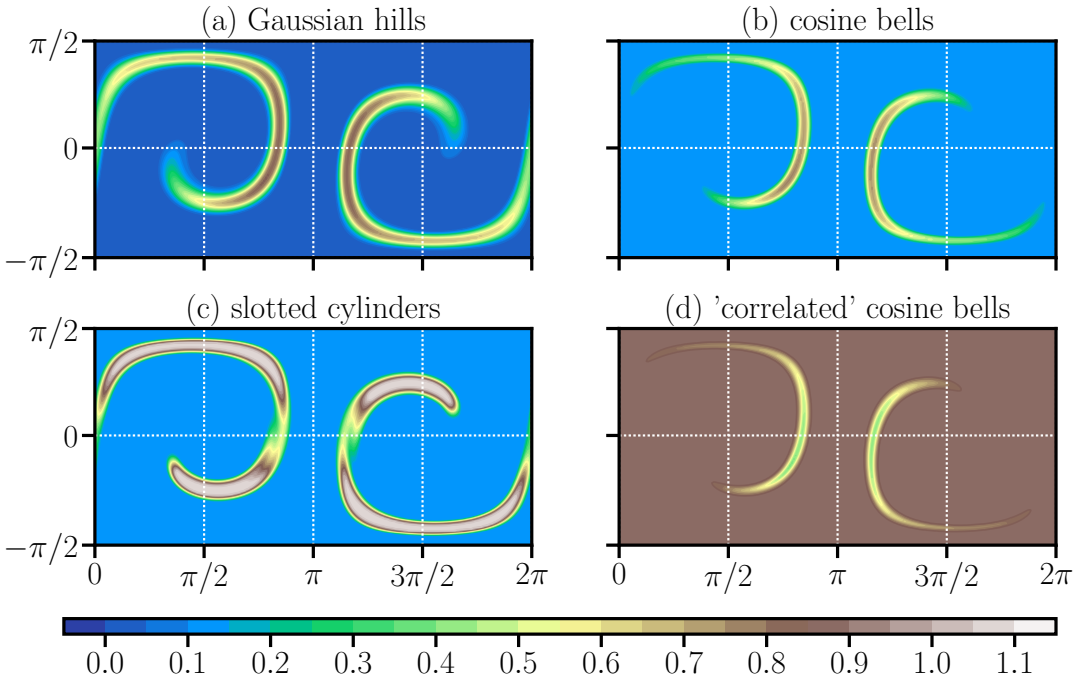

Fig. 5.4. Tracer fields for the reversing deformational flow at the time of the maximal deformation. The results were obtained using the Mg3No scheme on a grid with $N = 120$ ($\delta\lambda = 1.5°$), see Section 5.4 for details.

The first quantitative metric is the convergence in the ℓ_2 error norm with the increasing resolution using the Gaussian hill initial condition, presented in Figure 5.5.

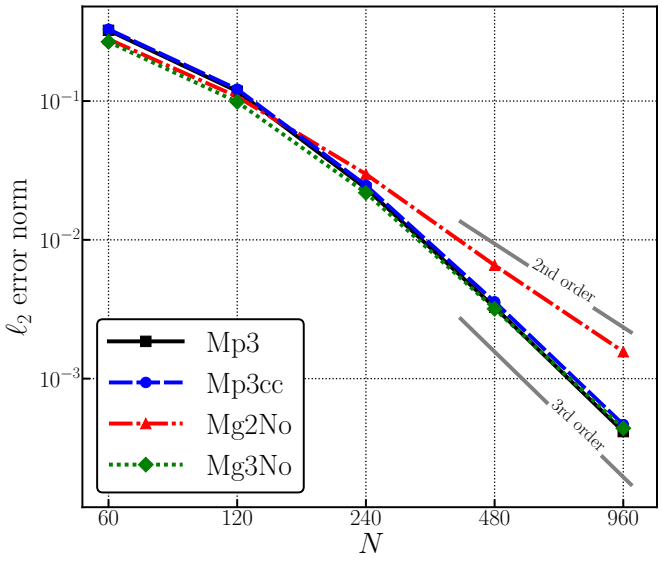

Fig. 5.5. Numerical convergence for the Gaussian hills initial condition of the reversing deformational flow test in the ℓ_2 error norm. The error was evaluated when the tracer first returned to its initial position.

In a stark difference to the preceding example, the results obtained using the Mp3, Mp3cc and Mg3No schemes are nearly identical. Each of the aforementioned

schemes converges at the third-order with negligible differences in the error norm. The lack of improvement in accuracy with the fully third-order accurate scheme can be attributed to the compact $\mathcal{C}^\infty$ support of the initial conditions that leads to the filamentary structure of the solution during most of the simulation time. Consequently, there is a scale separation between the smooth large-scale flow variations and the sharper gradients of the transported tracer. The truncation error associated with the flow variability is therefore much smaller than the error due to the tracer gradients, the latter of which is fully compensated to third-order by both the Mp3cc and Mp3 schemes. This hypothesis was tested by repeating the convergence test using the initial condition of the previous example in the considered flow field, resulting in the Mp3 scheme converging at the third order and the Mp3cc scheme falling off the third-order convergence line. Without cross-polar transport, the nonoscillatory scheme Mg3No retains the third-order convergence due to the MPDATA nonscillatory option blending first- and higher-order schemes with consistently low phase errors (Smolarkiewicz and Grabowski, 1990).

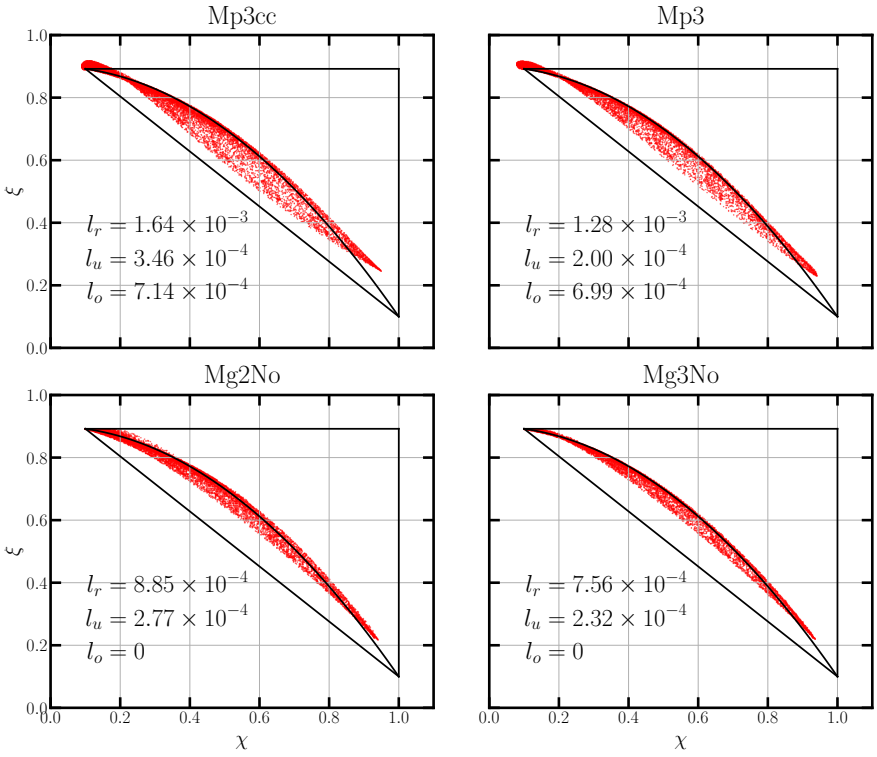

Fig. 5.6. Scatter plots showing preservation of the pre-existing functional relation for the reversing deformational flow test. The results for the 'correlated' cosine bells (ξ) versus cosine bells (χ) are shown at the time of the maximal deformation on a grid with $N = 240$ ($\delta\lambda = 0.75°$). The solid lines indicate the regions used to classify the numerical mixing. The mixing diagnostics ℓ_r, ℓ_u, ℓ_o are given for each scheme. See Section 5.4 for details.

Motivated by transport of long-lived species in the stratosphere or aerosol-cloud interactions, the authors in Lauritzen et al. (2012) included a set of diagnostics that

assess the ability of a scheme to preserve "pre-existing" functional relations. The setup involves the cosine bell initial conditions and another initial condition constructed from it, dubbed 'correlated' cosine bells. The construction is based on applying pointwise the non-linear functional relation $\xi(\chi) = -0.9\chi^2 + 0.8$ where χ is the value of the cosine bells tracer. Ideally, this relation should be preserved during the simulation, the correlation plot of ξ and χ plotted at the time of the maximal deformation shows the degree of numerical mixing introduced by the scheme. Furthermore, the numerical mixing can be classified into mixing resembling real mixing in the atmosphere, "range-preserving" unmixing and overshooting, which are quantified by the corresponding ℓ_r, ℓ_u and ℓ_o measures (Lauritzen and Thuburn, 2012).

Figure 5.6 presents the correlation plot and the numerical mixing measures for the four schemes considered in this example, computed on the grid with the $\delta\lambda = 0.75°$ intervals. The Mp3 scheme shows less of both the "real" mixing and the unmixing compared to the Mp3cc scheme. As both schemes are only sign-preserving they show some degree of overshooting, similar in magnitude. The overshooting is entirely eliminated by the nonoscillatory Mg2No and Mg3No schemes, that also exhibit smaller values of "real" mixing. Both "real" mixing and "range-preserving" unmixing diagnostics are better for the Mg3No scheme featuring the full third-order corrections. The measure of unmixing is similar with the Mp3 scheme and its nonoscillatory infinite-gauge counterpart Mg3No. The results presented here can be compared to the results obtained using a variety of state-of-the-art schemes in Lauritzen et al. (2014), section 3.5 therein. For example, values for the shape-preserving versions of the MPAS and the CAM-FV advection schemes at $\delta\lambda = 0.75°$, which can be directly compared to Mp3No, are $(l_r, l_u, l_o) = (6.43 \times 10^{-4}, 3.06 \times 10^{-4}, 0)$ and $(l_r, l_u, l_o) = (3.11 \times 10^{-4}, 1.98 \times 10^{-4}, 6.86 \times 10^{-5})$.

6 Fluid dynamics applications

This chapter substantiates the significance of the new development beyond the passive tracer advection. First, a synopsis of the MPDATA-based flow solvers, widely documented in the literature (Prusa et al., 2008; Smolarkiewicz and Charbonneau, 2013; Smolarkiewicz et al., 2014, 2016), is presented. Then, two problems, that utilise the full machinery of MPDATA-based solvers for anelastic flows, are considered. The first problem is a double sheer layer rollup in the framework of two-dimensional viscous Navier-Stokes equations. The charm of the problem is its relative simplicity, together with the discriminating accuracy indicator of producing (or not) at coarse resolutions superfluous eddies compared to pristine converged result with two eddies (Drikakis and Smolarkiewicz, 2001; Drikakis et al., 2002). The second problem is a three-dimensional simulation of dry convective boundary layer. It is a classical test for LES studies of atmospheric flows and the first experiment that demonstrated ILES capabilities of second-order accurate MPDATA (Margolin et al., 1999). Here, it is used to highlight benefits of the fully third-order MPDATA for simulating nonhydrostatic atmospheric flows, and to study its ILES properties.

6.1 MPDATA based integrator for an archetype fluid problem

In simulation of fluid dynamics, the prognostic governing PDEs can be viewed as a system of nonlinear inhomogeneous transport equations

$$\frac{\partial G\Psi}{\partial t} + \nabla \cdot (\boldsymbol{V}\Psi) = GR, \tag{6.1}$$

with the rhs forcings GR generally dependent on all prognostic variables. Given a fully second-order accurate forward-in-time advection algorithm for the homogeneous transport problem (2.1), written in short as

$$\Psi_i^{n+1} = \mathcal{A}_i(\Psi^n, \mathbf{V}^{n+1/2}, G) \ , \tag{6.2}$$

the inhomogeneous problem (6.1) is integrated to the second-order accuracy with the template algorithm

$$\Psi_{\boldsymbol{i}}^{n+1} = \mathcal{A}_{\boldsymbol{i}}(\Psi^n + 0.5\delta t R^n, \mathbf{V}^{n+1/2}, G) + 0.5\delta t R_{\boldsymbol{i}}^{n+1} \ , \tag{6.3}$$

provided at least $\mathcal{O}(\delta t^2)$ estimates of the advective velocity $\mathbf{V}^{n+1/2}$ and the rhs forcing R^{n+1} (Smolarkiewicz and Margolin, 1993; Smolarkiewicz, 2006; Smolarkiewicz et al., 2014). Advecting half of the rhs' trapezoidal integral effectively adds to the solution the term $-\delta t G^{-1}\nabla\cdot(0.5\delta t \mathbf{V} R)$ that compensates, to the second-order accuracy, the first-order truncation error term revealed by the Cauchy-Kowalevski procedure employed in derivation of the MPDATA integrator for the inhomogeneous transport problem (Smolarkiewicz and Margolin, 1993). Assuring fully third-order-accurate solutions to a complete system of fluid equations requires accounting for such coupling terms as well as fully third-order-accurate representation of the rhs. This may be virtually impossible in a paradigm of essentially two-time-level integrators. Moreover, the requirements such as the solution monotonicity (Smolarkiewicz and Grabowski, 1990), compatibility of scalar conservation laws with their Lagrangian forms (Kühnlein et al., 2012; Smolarkiewicz et al., 2016, 2017), or compatibility of elliptic Poisson/Helmholtz operators with advection (Smolarkiewicz et al., 2014) may take precedence over the formal accuracy, for the sake of physical realisability and efficacy in complex simulations. Nevertheless, the increased accuracy of the homogeneous algorithm $\mathcal{A}_{\boldsymbol{i}}$ can benefit the overall accuracy of integrations, as evidenced by the subsequent examples.

6.2 Governing equations

The problems considered in this chapter assume the incompressible Boussinesq limit of the all-scale Euler equations Smolarkiewicz et al. (2014). Assuming a quiescent environment with background potential temperature $\Theta(z)$ such that $\Theta(z=0) = \Theta_o =$ const., and density $\rho(z) = \rho_o =$ const., the governing Boussinesq PDEs in a Cartesian reference frame are compactly written as

$$\begin{aligned}
&\frac{\partial \mathbf{u}}{\partial t} + \nabla\cdot(\mathbf{u}\otimes\mathbf{u}) = -\nabla\varphi - \mathbf{g}\frac{\theta}{\Theta_o} + \boldsymbol{\mathcal{D}}_{\boldsymbol{u}} \ , \\
&\frac{\partial \theta}{\partial t} + \nabla\cdot(\mathbf{u}\theta) = -\mathbf{u}\cdot\nabla\Theta + \mathcal{D}_\Theta \ , \\
&\nabla\cdot\mathbf{u} = 0 \ .
\end{aligned} \tag{6.4}$$

Here, $\mathbf{u} = (u^1, u^2, u^3)$ and θ denote velocity vector and potential temperature perturbation with respect to the ambient state, φ is the density normalised pressure perturbation and $\mathbf{g} = (0, 0, -g)$ marks the gravitational acceleration. The terms $\boldsymbol{\mathcal{D}}_{\boldsymbol{u}}$ and $\mathcal{D}_\Theta$ refer to dissipative and diabatic forcings in the momentum and entropy equations, respectively. The equations of the system (6.4) are of the form (6.1)—with $G \equiv \rho_o$, Ψ corresponding

to θ and components of $\mathbf{u}$, and R representing the associated rhs—whereby integrations of (6.4) adopt the template algorithm (6.3).

Completing the solution to (6.4) requires combining templates (6.3) for θ and vertical velocity component u^3 into the closed form expression for $\mathbf{u}|^{n+1}$, subsequently plugged into the discrete form of the mass continuity equation of (6.4) to generate the elliptic boundary value problem for φ, see Smolarkiewicz et al. (2014, 2016) for details. For compatibility of θ advection with the elliptic solver, $\alpha \equiv 0$ in (3.12)[1].

6.3 Viscous rollup of a double shear layer

Following Brown and Minion (1995); Minion and Brown (1997), the rollup of a double shear layer has become an accuracy benchmark for assessing the performance of various of numerical methods designed to integrate incompressible Navier-Stokes equations. The governing equations are a special case of (6.4) with identically vanishing g, θ and $\mathcal{H}$, while $\boldsymbol{\mathcal{D}}_{\boldsymbol{u}} = \nu\Delta\boldsymbol{u}$ is the incompressible viscous stress and ν denotes the viscosity.

The dimensionless problem is posed on a 2D doubly-periodic Cartesian domain of a unit linear extent, with the divergence free initial condition

$$u^1 = \begin{cases} \tanh((y-0.25)\delta) \text{ if } y \leqslant 0.5 \\ \tanh((0.75-y)\delta) \text{ otherwise,} \end{cases} \tag{6.5}$$

$$u^2 = v' \sin(2\pi x). \tag{6.6}$$

The parameter δ controls the thickness of the shear layer, here $\delta = 100$ results in a relatively thick layer. A small perturbation of magnitude $v' = 0.05$ is added to the second velocity component to trigger the flow evolution. The chosen value of the viscosity $\nu = 0.5 \cdot 10^{-4}$ corresponds to the Reynolds number Re$= 10^4$.

The problem was discretised on a $N \times N$ regular Cartesian grid. All simulations were run for $N = 129, 257, 513, 1025, 2049$ to asses convergence. The simulations used a constant time step $\delta t = 0.8\delta x$ and the final time was $t = 1.5$. Here and in the following section, simulations using the nonoscillatory infinite-gauge variants of, respectively, the second-order accurate (Mg2No), the third-order constant coefficient (Mg3ccNo) and the fully third-order accurate (Mg3No) MPDATA were performed. Advective velocities were linearly extrapolated to the intermediate time level and interpolated to cell faces.

The idea of the double shear-layer benchmark is that its under-resolved simulations feature artefacts in the form of spurious vortices, which, without knowledge of the resolved solution, could be mistaken for physical features. With this respect, Fig. 6.1 is self-evident showing for the same grid the increased accuracy of the solutions based on

[1]The elliptic solver uses a second-order accurate discretisation of the incompressibility constraint. Without setting $\alpha \equiv 0$ this result in incompatibility with the fully third-order accurate scheme, which manifests itself as spurious oscillations in constant background states.

the fully third-order-accurate advection solver.

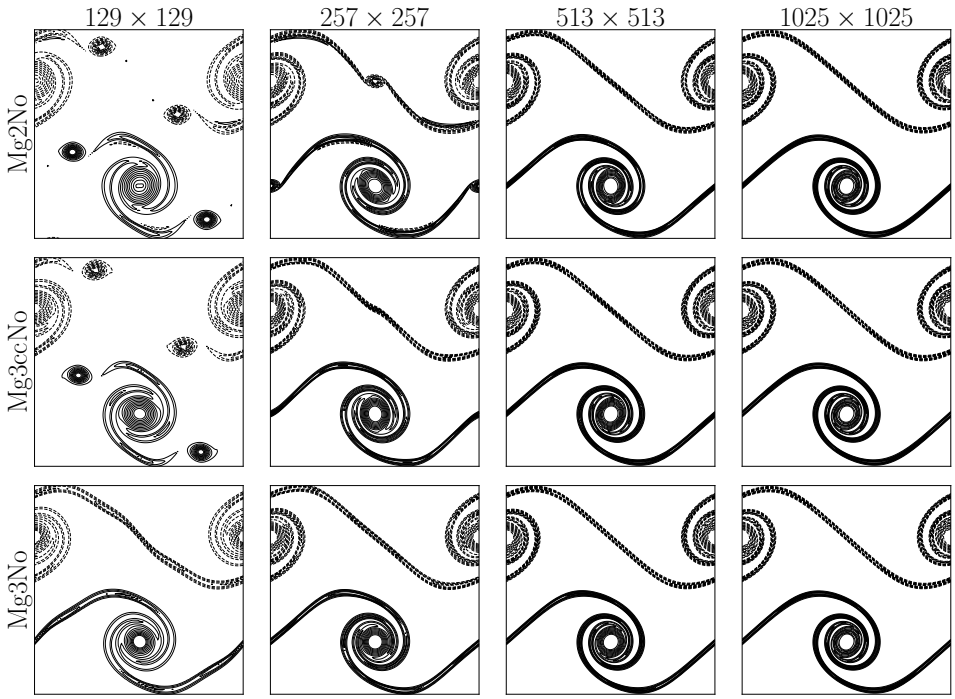

Fig. 6.1. Vorticity isolines for Mg2No, Mg3ccNo and Mg3No advection (top to bottom) for 129×129, 257×257, 513×513 and 1025×1025 doubly periodic grids (left to right).

Tabela 6.1
Error norm ℓ_2 of u^1 velocity component for the double shear layer example calculated at $t = 1.5$. Reference solution was obtained on a 2049×2049 grid with Mg3No.

Grid	Mg2No	Order	Mg3ccNo	Order	Mg3No	Order
129×129	3.35×10^{-1}	—	3.65×10^{-1}	—	7.02×10^{-2}	—
257×257	1.96×10^{-1}	0.77	1.09×10^{-1}	1.74	4.79×10^{-2}	0.55
513×513	7.21×10^{-2}	1.44	2.90×10^{-2}	1.91	1.57×10^{-2}	1.60
1025×1025	2.05×10^{-2}	1.82	7.06×10^{-3}	2.04	4.30×10^{-3}	1.87

Table 6.1 quantifies the accuracy of the selected MPDATA options and corroborates the discussion of the preceding subsection. While for each resolution the Mg3No scheme is consistently the most accurate, the convergence rate of all schemes appears to approach the second-order asymptotic limit; however this is not formally ensured as the diffusion terms are integrated only to $\mathcal{O}(\delta t^2)$. The quickest accuracy gain of the Mg3ccNo result is correlated with its largest error at the coarse resolution where the solution is topologically inconsistent with the converged result.

6.4 ILES of convective boundary layer

The problem of turbulent convective planetary boundary layer in the Boussinesq limit was one of the first demonstrations of the ILES property of MPDATA-based flow solvers (Margolin et al., 1999). Here this experiment is adopted to investigate the ILES properties of the fully third-order accurate MPDATA and show its benefits for simulations of nonhydrostatic atmospheric dynamics. The calculations closely follow the setup of Smolarkiewicz et al. (2013), which is briefly summarised below.

The equations (6.4) assume prescribed diabatic forcings $\mathcal{D}_{\boldsymbol{u}} = -d\boldsymbol{\tau}/dz$ and $\mathcal{D}_\theta = -dH/dz$, where $\boldsymbol{\tau}$ and H represent fluxes of momentum and heat, respectively. Both fluxes are parametrised similarly, $\boldsymbol{\tau} = \boldsymbol{\tau}_o \exp(-z/\lambda)$ and $H = H_o \exp(-z/\lambda)$, with the surface drag $\boldsymbol{\tau}_o = -C_d \|\boldsymbol{u}_o\| \boldsymbol{u}_o$, the surface heat flux $H_o = 0.01\ \mathrm{K\,m\,s^{-1}}$, the drag constant $C_d = 0.1$, and the length scale $\lambda = 25$ m. Since the fluxes decay exponentially with height, they parametrise only near-surface effects, whereas ILES properties of MPDATA are responsible for subgrid-scale modelling aloft. The ambient $\Theta(z) = 300$ K up to 500 m and $\Theta(z) = \Theta_o[1 + Sz]$ above, with the stratification $S = 10^{-5}\ \mathrm{m^{-1}}$. The model domain of size 3200 m $\times$ 3200 m $\times$ 1500 m is periodic in horizontal with rigid-lid boundaries at the top and the bottom. Gravity wave absorbers attenuate the solution toward ambient conditions in the vicinity of the upper boundary, with a time scale that increases linearly from 0 at the distance 500 m below the boundary to $1020^{-1}\ \mathrm{s^{-1}}$ at the boundary. The initial conditions are generated by randomly perturbing θ and $w := u^3$ with a small amplitude white noise and then finding the potential flow consistent with mass continuity. The amplitude of the perturbation at the surface is 0.001 K and $0.2\ \mathrm{m\,s^{-1}}$, respectively for θ and w, and decreases linearly with height to zero at the top of the mixed layer.

The model domain was discretised on a $65 \times 65 \times 51$ regular Cartesian grid, corresponding to horizontal grid spacings $\delta x = \delta y = 50$ m and a vertical grid spacing $\delta z = 30$ m. To allow statistical analysis of the inherently sensitive turbulent flow, for every MPDATA variant an ensemble of 60 simulations was performed, each initialised with a different white noise perturbation. The final-time profiles and spectra presented below were averaged over this ensemble, as well as over the last 50 time steps of simulation. All simulations were run with a constant time step $\delta t = 8$ s for 15000 s, corresponding to about 13 large eddy-turnover times.

Figure 6.2 shows profiles of heat flux, temperature variance, and vertical velocity variance, generated with nonoscillatory infinite-gauge options of the second-order-accurate, third-order-accurate for constant coefficients and fully third-order accurate MPDATA. For comparison purposes, experimental data and results from a reference LES study of Schmidt and Schumann (1989) are also presented. Overall, the profiles for different MPDATA options are similar, confirming that the fully third-order is also capable of ILES. Moreover, the standard convective scales are independent of advection

scheme. Their values $z_i = 690$ m, $w^* = 0.613\ \mathrm{m\,s^{-1}}$, $t^* = 1126.2$ s and $T^* = 0.0163$ K closely match those in the first row of Table 1 in Smolarkiewicz et al. (2013). As the accuracy of the advection scheme increases, the vertical velocity evinces amplification of the variance.

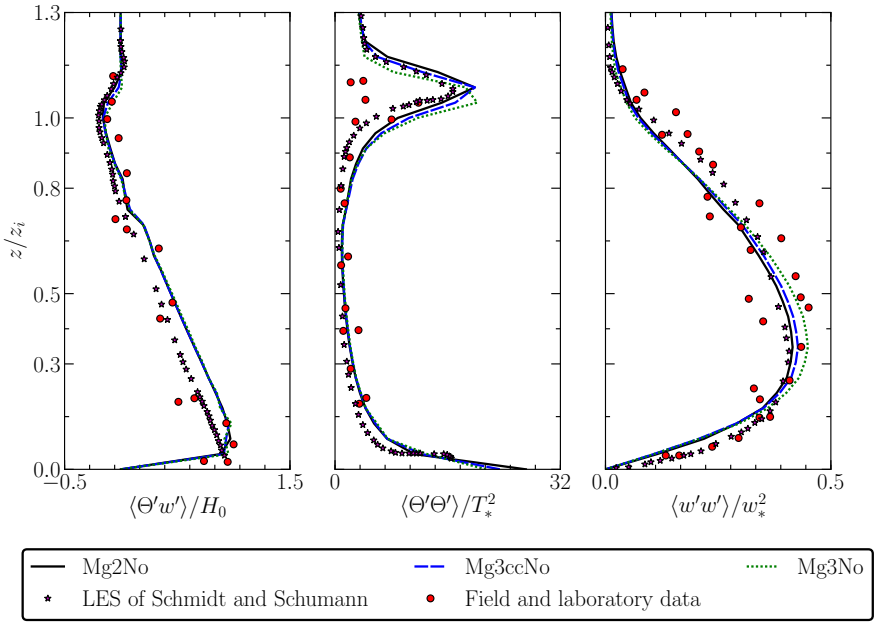

Fig. 6.2. Normalised profiles (at $t/t^* \approx 13$ large-eddy turnover times) of heat flux, temperature variance, and vertical velocity variance, in ILES simulations of the convective boundary layer, employing Mg2No, Mg3ccNo and Mg3No advection; stars denote the explicit LES result of Schmidt and Schumann (1989) generated with second-order-accurate centred-in-space differencing, and red circles represent field and laboratory data. The profiles were averaged over a short time-window and ensemble of simulations, see the text for details.

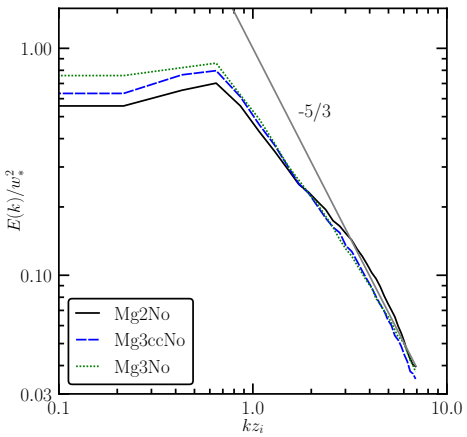

Fig. 6.3. Normalised vertical velocity spectra (at $t/t^* \approx 13$ and $z/z_i = 0.4$) in ILES simulations of the convective boundary layer, employing Mg2No, Mg3ccNo and Mg3No advection. The spectra were averaged over a short time-window and ensemble of simulations, see the text for details.

Further effects of increasing the order of accuracy can be observed on the power spectra of vertical velocity presented in Figure 6.3. The spectra show increasing length of the inertial range and more energy in the largest scales with increasing order. The changes in vertical velocity variance and spectra are consistent with increasing effective resolution of the simulation (cf. Figs. 6-8 in Sullivan and Patton (2011)) or, alternatively, the effective Reynolds number; see §6.5.7 in Pope (2000).

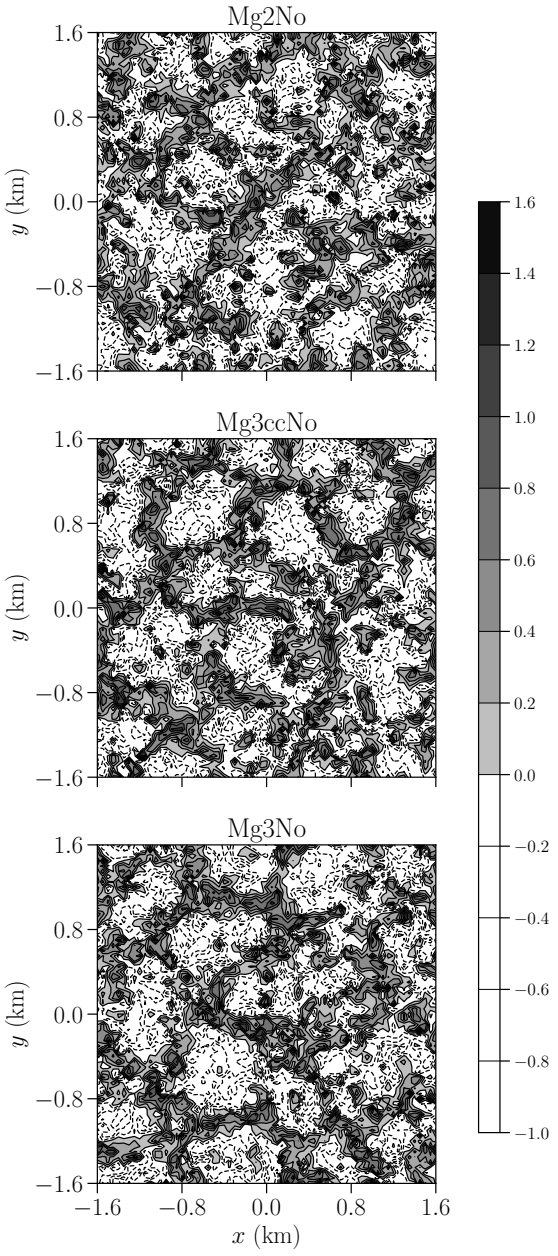

Fig. 6.4. Vertical velocity field u^3 [$\mathrm{m\,s^{-1}}$] in the $x-y$ plane at $z/z_i \approx 0.2$ and $t/t^* \approx 13$, using Mg2No, Mg3ccNo and Mg3No advection.

Furthermore, Fig. 6.4 shows the instantaneous vertical-velocity field organized into characteristic Rayleigh-Bénard cells (Piotrowski et al., 2009) evincing improved regularity for the full third-order accuracy, as opposed to the constant-coefficient case of the MPDATA advection. Nonetheless both are superior to the Mg2No solution. The latter result indicates that the implicit subgrid-scale model contained in the truncation terms of the Mg3No scheme may be even more scale selective than in second-order MPDATAs (Domaradzki et al., 2003; Strugarek et al., 2016); cf. §3.3 in Schmidt and Schumann (1989) for a discussion. Notwithstanding the improvements in the solution quality with the increasing accuracy of the MPDATA advection, all three results are formally at most second-order-accurate.

7 Idealised supercell simulations

The previous chapter compared the fully third-order-accurate MPDATA to second-order variants for simulating dry atmospheric dynamics in the nonhydrostatic regime. Here, another comparison is presented for a significantly more complicated case of moist precipitating dynamics. Specifically, simulations of an idealised supercell storm were performed, which is a classical benchmark case for studies of deep moist convection (Klemp and Wilhelmson, 1978; Smolarkiewicz et al., 2017)

Supercells are intense long-lived convective storms characterised by persistent rotating updraughts (Klemp, 1987). High values of convective available potential energy and the presence of strong low-level environmental wind shear are conducive to supercell formation. Vorticity dynamics plays a key role in the evolution of supercell storms. Twisting of vortex tubes by precipitation-laden downdraughts may lead to storm splitting, a distinctive phenomenon where a single supercell separates into two counterrotating storms. Supercell storms often produce severe weather such as damaging wind, large hail, and the world's most intense tornadoes.

Simulations of supercell thunderstorms are challenging because latent heat release injects energy at the finest scales, which are highly susceptible to numerical errors. To regularise the smallest scales idealised studies of supercells often introduce simple diffusive terms that are a proxy for full model physics. Results of simulations are sensitive to the form and magnitude of introduced dissipation and to numerical details (Kurowski et al., 2011, 2014).

Recently, a supercell benchmark was formulated on a reduced-radius sphere (Klemp et al., 2015) and adopted for an intercomparison project of global atmospheric models (Ullrich et al., 2017). To allow grid-convergence studies, the benchmark assumes constant coefficients of diffusion and viscosity. The preliminary results of the intercomparison (Zarzycki et al., 2018) show very large intermodel differences, further confirming high sensitivity of results to numerical formulation. For each individual model, convergence was observed when approaching 0.5 km horizontal grid spacing. Inspired by the benchmark, a similarly posed problem is used to investigate benefits of the fully third-order accurate MPDATA for supercell simulations.

7.1 Governing equations

To properly describe deep convection the previously presented Boussinesq equations (6.4) are extended to a fully anelastic system, assuming height-dependant base state profiles of density $\rho_b(z)$ and potential temperature $\theta_b(z)$. The treatment of moisture is based on one-moment bulk microphysics, with new primary variables q_v, q_c, q_p denoting mixing ratios of water vapour, cloud water, and precipitation, respectively. The equations are written in conservation form as

$$\frac{\partial \boldsymbol{u}}{\partial t} + \frac{1}{\rho_b}\nabla\cdot(\rho_b \boldsymbol{u}\otimes\boldsymbol{u}) = -\nabla\varphi - \frac{\boldsymbol{g}}{\theta_b}\left(\theta' + \theta_b(\varepsilon q_v' - q_c - q_p)\right) + \boldsymbol{\mathcal{D}}_{\boldsymbol{u}}, \tag{7.1}$$

$$\frac{\partial \theta'}{\partial t} + \frac{1}{\rho_b}\nabla\cdot(\rho_b \boldsymbol{u}\theta') = -\mathbf{u}\cdot\nabla\theta_e + \frac{L\theta_e}{c_p T_e}(C_d + E_p) + \mathcal{D}_\theta, \tag{7.2}$$

$$\frac{\partial q_v}{\partial t} + \frac{1}{\rho_b}\nabla\cdot(\rho_b \boldsymbol{u} q_v) = -C_d - E_p + \mathcal{D}_{q_v}, \tag{7.3}$$

$$\frac{\partial q_c}{\partial t} + \frac{1}{\rho_b}\nabla\cdot(\rho_b \boldsymbol{u} q_c) = C_d - A_p - C_p + \mathcal{D}_{q_c}, \tag{7.4}$$

$$\frac{\partial q_p}{\partial t} + \frac{1}{\rho_b}\nabla\cdot(\rho_b \boldsymbol{u} q_p) = A_p + C_p + E_p + \mathcal{D}_{q_p} - \frac{1}{\rho_b}\nabla\cdot(\rho_b \boldsymbol{u}_\downarrow q_p), \tag{7.5}$$

$$\nabla\cdot(\rho_b\boldsymbol{u}) = 0. \tag{7.6}$$

Here, T denotes the temperature, L is the latent heat of condensation, c_p is the specific heat at constant pressure, $\varepsilon = R_v/R_d - 1$, where R_v/R_d is the ratio of the gas constants for water vapour and dry air. The primed variables denote perturbations from environmental profiles marked by the subscript e, that is $\Psi' = \Psi - \Psi_e$. The microphysical source terms include condensation of water vapour into cloud water (C_d), autoconversion of cloud water into precipitation (A_p), collection of cloud water by precipitation (C_p), and evaporation of precipitation in the undersaturated conditions (E_p). Additionally, the terms D_{q_i} symbolise dissipative forcings for water species, such as molecular or eddy diffusion. The last term on the rhs of (7.6) describes the precipitation fallout with the velocity $\boldsymbol{u}_\downarrow = (0, 0, -w_t)$ where w_t is the terminal velocity.

The parametrisation of microphysical processes assumes a standard warm-rain formulation, summarised in Appendix B. For details of coupling the microphysics to the dynamics during numerical integration the reader is refereed to the review in Smolarkiewicz et al. (2017).

7.2 Simulation setup

Setup of idealised supercell simulations usually includes two key ingredients—environmental profiles of wind, temperature, and moisture conducive to supercell formation and a smooth localised initial perturbation of temperature. Here, the setup of Klemp et al. (2015) is used, modified from spherical geometry to a flat plane.

The size of the domain is $L_x \times L_y \times L_z = 168$ km $\times 168$ km $\times 20$ km. Rigid boundaries are assumed at the top and bottom of the domain, whereas lateral boundaries are periodic. The environmental potential temperature profile is prescribed by

$$\theta_e(z) = \begin{cases} \theta_o + (\theta_{tr} - \theta_o)\left(\frac{z}{z_{tr}}\right)^{5/4} & \text{for } z \leqslant z_{tr} \\ \theta_{tr} \exp\left[\frac{g}{c_p T_{tr}}(z - z_{tr})\right] & \text{for } z > z_{tr}, \end{cases} \tag{7.7}$$

where $\theta_o = 300$ K is the surface potential temperature, $\theta_{tr} = 343$ K is the potential temperature at the tropopause level of height $z_{tr} = 12$ km, and $T_{tr} = 213$ K is the temperature of the isothermal stratosphere. The water content is given by the relative humidity profile

$$H_e(z) = \begin{cases} 1 - \frac{3}{4}\left(\frac{z}{z_{tr}}\right)^{5/4} & \text{for } z \leqslant z_{tr} \\ \frac{1}{4} & \text{for } z > z_{tr}. \end{cases} \tag{7.8}$$

Additionally, the initial water vapour mixing ratio is constrained by $q_{v0} = \max\left(q_{v0}, q_{v0}^{max}\right)$ with $q_{v0}^{max} = 0.014$ kg kg^{-1} to approximate a well-mixed boundary layer near the ground. The environmental wind is $\boldsymbol{u}_e = (U_e(z), 0, 0)$, with the zonal velocity profile

$$U_e(z) = \begin{cases} U_s\left(\frac{z}{z_s}\right) - U_c & \text{for } z \leqslant z_s - \Delta z_s \\ U_s\left[-\frac{4}{5} + 3\frac{z}{z_s} + \frac{5}{4}\left(\frac{z}{z_s}\right)^2\right] - U_c & \text{for } |z - z_s| < \Delta z_s \\ U_s - U_c & \text{for } z > z_s + \Delta z_s, \end{cases} \tag{7.9}$$

where $U_s = 30$ m s^{-1}, $z_s = 12$ km, $\Delta z_s = 1$ km, and $U_c = 15$ m s^{-1} accounts for a Galilean shift to render the storm nearly stationary. The initial potential temperature perturbation is

$$\delta\theta = \begin{cases} \Delta\theta \cos\left(\frac{\pi R}{2}\right) & \text{for } R \leqslant 1 \\ 0 & \text{for } R > 1, \end{cases} \tag{7.10}$$

where

$$R(x, y, z) = \sqrt{\left(\frac{x - x_0}{R_x}\right)^2 + \left(\frac{y - y_0}{R_y}\right)^2 + \left(\frac{z - z_0}{R_z}\right)^2}. \tag{7.11}$$

Here, the magnitude of the perturbation is $\Delta\theta = 3$ K, $(x_0, y_0, z_0) = (L_x/2, L_y/2, R_z)$, where $R_x = R_y = 10$ km and $R_z = 3.5$ km.

As mentioned at the beginning of the chapter, the assumed form of dissipation is important. The adopted setup assumes constant viscosity $\nu = 500$ m^2 s^{-1} for momentum

and a common diffusion coefficient $K_s = 1500\ \mathrm{m^2\,s^{-1}}$ for all scalar variables. To prevent mixing of the geostrophically balanced environmental state, the dissipation and diffusion are only applied to the perturbations about it.

The domain was discretised with vertical grid spacing $\delta z = 0.5$ km. For the purpose of grid-refinement study, four different horizontal spacings were used $\delta x = \delta y = 4, 2, 1,$ and 0.5 km. The time step was continuously adapted to keep the Courant number smaller than 0.8, and the total simulation time was two hours. Simulations using the fully third-order scheme and the second-order MPDATA were performed, both in the nonoscillatory infinite-gauge configuration.

7.3 Results

Figure 7.1 illustrates the evolution of the storm over the two hour period; the result was obtained using the fully third-order accurate MPDATA on the finest grid with 0.5 km spacing. This result compares well to Figure 3 in Smolarkiewicz et al. (2017), which was also obtained using MPDATA-based numerics. The figure presents characteristic splitting of the storm, showing two separate convective cells past the 30 min mark.

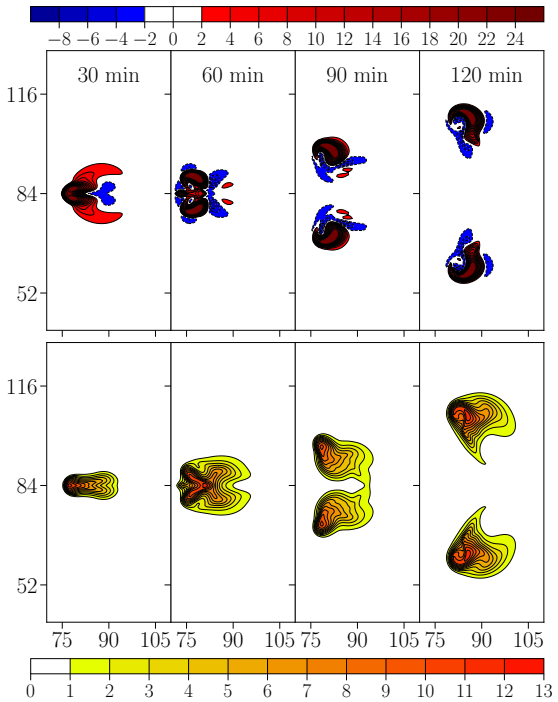

Fig. 7.1. Supercell evolution in the simulation using the Mg3No scheme at 0.5 km resolution. Horizontal cross sections of vertical velocity (top; $\mathrm{m\,s^{-1}}$) and rainwater mixing ratio (bottom; $\mathrm{g\,kg^{-1}}$) at 5 km altitude in 30 min intervals.

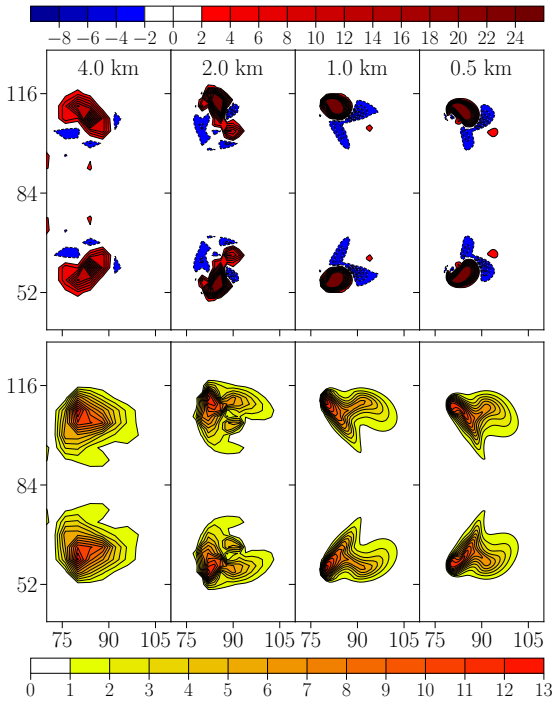

Fig. 7.2. Horizontal cross sections of the final (at 120 min) vertical velocity (top; $\mathrm{m\,s^{-1}}$) and rainwater mixing ratio (bottom; $\mathrm{g\,kg^{-1}}$) at 5 km altitude for grid spacings 4 km, 2 km, 1 km, and 0.5 km (left to right). Results from simulations employing the Mg2No scheme.

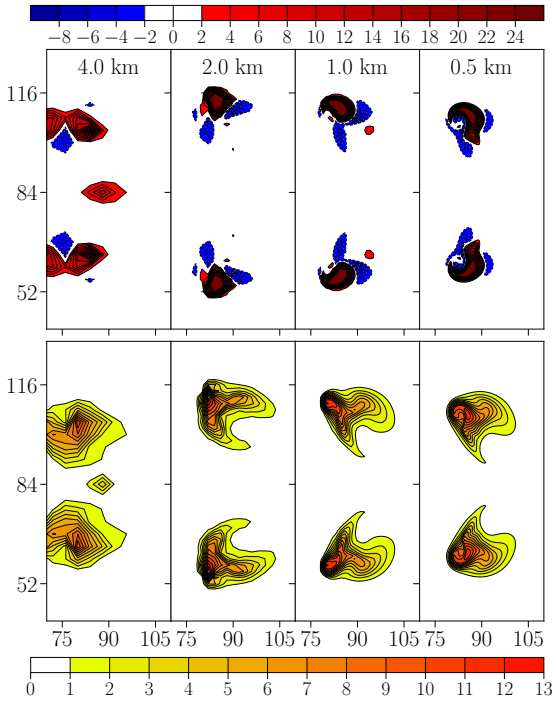

Fig. 7.3. Same as Figure 7.2 but for simulations employing the Mg3No scheme.

Figures 7.2 and 7.3 show structural convergence under grid refinement of the final vertical velocity and rainwater distributions at 5 km altitude, for the second-order accurate scheme and the fully third-order accurate scheme, respectively. As expected, both options show increasing detail in the solution as the resolution increases. The 4 km solutions are clearly under-resolved. While both 2 km solutions do not appear well-resolved, the solution using the fully third-order accurate scheme appears to have better effective resolution. Moreover, the vertical velocity distribution of the Mg3No scheme at 1 km grid spacing compares better to the Mg2No solution at 0.5 km grid spacing than to its 1 km equivalent. Interestingly, the updraught region of the Mg3No scheme becomes more elongated at 0.5 km grid spacing, and looks different than the corresponding Mg2No result, while the distributions of rainwater appear similar. However, all of the observed differences are small compared to the intermodel differences presented by the intercomparison in Zarzycki et al. (2018).

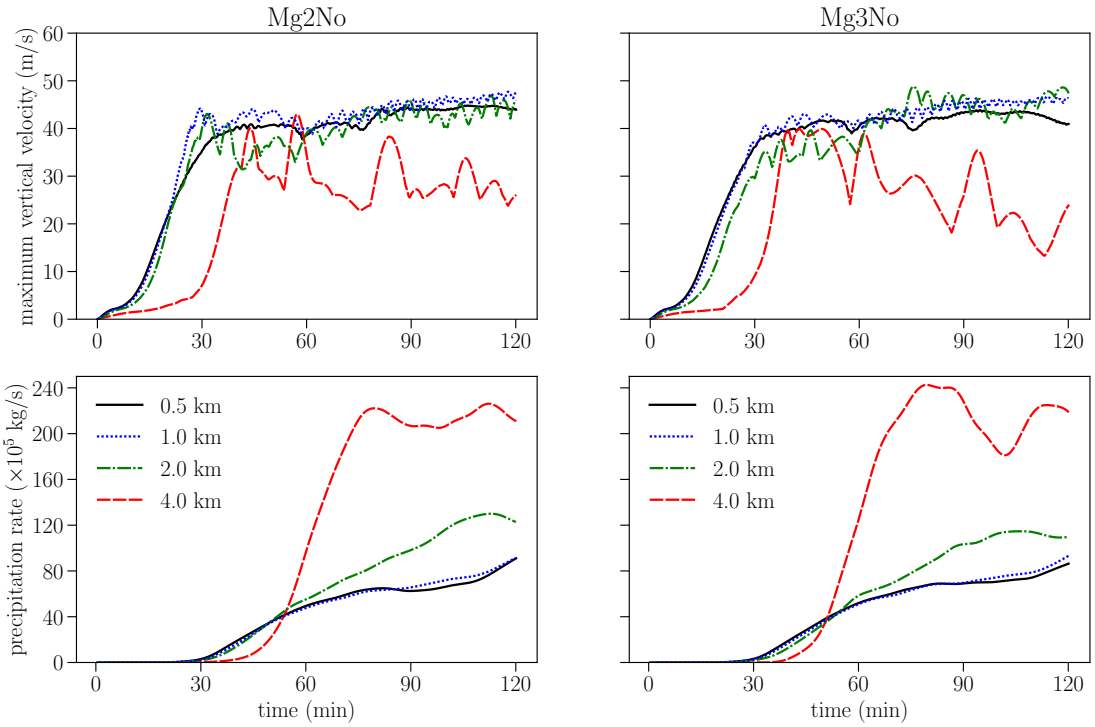

Fig. 7.4. Instantaneous maximum vertical velocity and precipitation rate time series for the Mg2No (left) and the Mg3No (right) supercell simulations with different grid spacings.

Time series of maximal vertical velocity and precipitation rate for every considered grid spacing and MPDATA variant are presented in Figure 7.4. The plots further corroborate that 4 km solutions are under-resolved, showing much too small (large) vertical velocity (precipitation rate) values. The time series at 2 km grid spacing improve upon these results, but visibly are not yet converged. The Mg3No scheme at 2 km shows a bit larger vertical velocity maxima and smaller precipitation rates than the

corresponding Mg2No solution during the second hour of the simulation. The statistics appear almost converged at 1 km grid spacing, which is especially evident by looking at the precipitation rates. At this resolution, the fully third-order MPDATA vertical velocity during the first hour of the simulation is similar to the 0.5 km result, while the second-order scheme overshoots its fine grid solution. Both MPDATA options show slightly higher vertical velocities than the fine grid solutions during the second hour of the evolution.

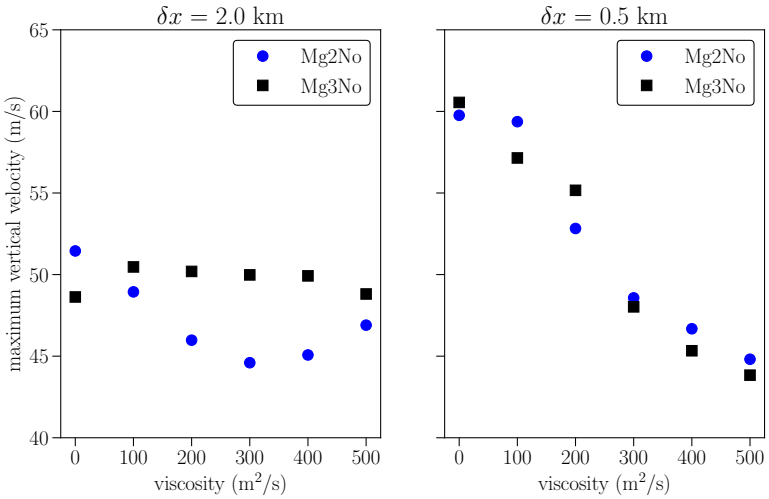

Fig. 7.5. Maximum vertical velocity for the entire simulation as a function of the viscosity magnitude. Results from simulations with the Mg2No and the Mg3No MPDATA variants at 2 km (left) and 0.5 km (right) grid spacings are shown.

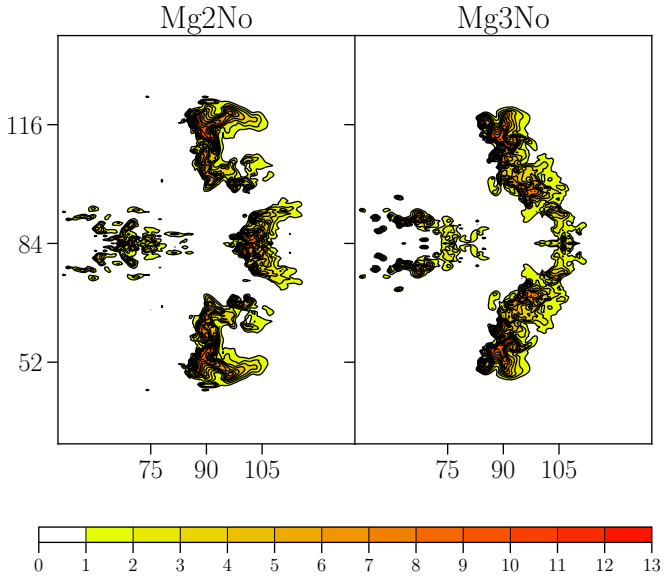

Fig. 7.6. Horizontal cross sections of the final (at 120 min) rainwater mixing ratio (g kg^{-1}) at 5 km altitude in inviscid 0.5 km grid spacing simulations using the Mg2No and the Mg3No MPDATA.

To further investigate differences between the Mg2No and Mg3No simulations, sensitivity analysis to modifying the viscosity magnitude was conducted, similarly as in Kurowski et al. (2014)—see their Section 4.c and Figure 8. Simulations with progressively smaller values of viscosity were performed, down to a formally inviscid case relying on the ILES property of MPDATA. Diffusion coefficients for the scalar fields were also proportionally reduced. Figure 7.5 presents the dependence of maximum (over the course of the entire simulation) vertical velocity on the viscosity coefficient for 2 km and 0.5 km grid spacings. At 2 km grid spacing, the Mg3No simulations shows consistently higher maximal updraught speeds for every value of viscosity except zero. However, the viscous term is not yet converged, as there is no clear trend of increasing updraught speeds with decreasing viscosity. The expected trend can be observed for 0.5 km simulations, but there is no systematic difference between the fully third MPDATA and the second order variant. Nonetheless, decreasing viscosity does lead to solutions showing different morphology, distinct for each scheme, as can be seen in Figure 7.6 comparing ILES solutions at 0.5 km. With that in mind, the maximum vertical velocity statistics do not tell the whole story, as numerical diffusivity exhibits a spatial structure. Real storms are characterised by much higher Reynolds numbers, and may benefit from the implicit subgrid-scale model of the fully third-order scheme. To sum up, the results suggest that using the fully third-order MPDATA has positive impact on the solutions when running on coarser resolutions, but the effect is overshadowed by the diffusive term which is not yet fully converged.

8 Final remarks

Advection schemes are a key element of numerical atmospheric models, which are essential for the state-of-the-art weather forecasting and research. The schemes' order of accuracy determines not only their effective resolving power, but also (and perhaps even more importantly) their behavioural properties.

The development of nonoscillatory second-order accurate advection schemes in the seventies and the eighties was transformative for the whole field of computational fluid dynamics, allowing realistic simulations of turbulent flows. During the same time, the generally second-order accurate MPDATA advection scheme emerged for atmospheric applications, incorporating favourable properties such as full multidimensionality and strict sign-preservation. Since that era, research into higher-order accurate advection algorithms has been ongoing, motivated by the desire to further diminish numerical errors and explore different behavioural characteristics.

While many high-order accurate schemes have been proposed, combining the nonoscillatory or sign-preserving properties with high-order of accuracy has proven difficult, either limiting many schemes applicability or forcing them to abandon their formal order of accuracy. In the meantime, the second-order MPDATA has become a foundation for general geo- and astrophysical flow solvers, enjoying a diverse area of applications and being praised for their robustness. The goal of the research presented in this thesis was to use the MPDATA approach to construct a genuinely third-order accurate advection scheme for atmospheric applications, while keeping the favourable properties of MPDATA.

A fully third-order accurate MPDATA advection scheme under a temporally and spatially varying flow has been developed. The foundation of the proposed scheme lies in the rigorous modified equation analysis of the standard MPDATA, followed by expressing the spatial form of the error as the divergence of an advective flux. The discrete error estimate is compensated in the subsequent upwind pass, resulting in a third-order-accurate sign-preserving scheme. The scheme requires only two upwind passes, which can benefit parallel distributed-memory communication.

The main building block of the proposed scheme is the third-order error-compensating pseudo-velocity, which was derived in a continuous form and later discretised on a structured rectilinear computational grid. To provide insight into the various sour-

ces of the standard MPDATA error, the pseudo-velocity was separated into select terms with a clear interpretation. Using a computer algebra system, the third-order error-compensating velocity was augmented with terms that compensate errors of common interpolation and extrapolation procedures in implementations of the standard MPDATA.

The developments presented in this thesis are available as part of the open-source *libmpdata++* library (Jaruga et al., 2015). The library implements a variety of MPDATA-based solvers and provides facilities for parallelisation and output. It is implemented in an object-oriented manner, benefiting user/researcher productivity and long-term code maintainability. As a side benefit of the presented work, many other enhancements to the library capabilities were added. The library was used to perform every simulation presented in the thesis.

Three-dimensional numerical convergence tests based on a manufactured solution verified the third-order accuracy of the scheme. Two benchmarks of tracer advection in time-varying rotating deformational flows on the sphere—pertinent to global chemistry-transport models—were used to compare the proposed scheme with the established MPDATA formulations. The novel third-order accurate MPDATA showed a robust decrease in the solution error compared to the established third-order constant-coefficient scheme. Moreover, the fully third-order scheme with nonoscillatory enhancement is substantially more accurate than the established nonoscillatory MPDATAs. The novel scheme can also much better preserve functional correlations between the tracers. Evaluation of the computational cost showed the efficacy of the fully third-order accurate MPDATA schemes, with about the same cost as the third-order constant-coefficient scheme.

In general, simulations of complete fluid equations for the rollup of a double shear layer, the evolution of a convective boundary layer, and the splitting of an idealised supercell storm reveal overall accuracy gains of the advective transport based on the fully third-order-accurate scheme. This is despite the fact that the complete model is at most second-order accurate, and, in addition to advective transport, feature increasingly complex physics. Specifically, the rollup of the double shear-layer allowed both visual and quantitative assessment of the solution accuracy, manifestly showing smaller errors of the fully third-order scheme. The evolution of the convective boundary layer revealed characteristics consistent with higher numerical resolution of the fully third-order scheme, while also demonstrating its advantageous ILES properties. Similarly, the splitting supercell benchmark benefited from the smaller numerical dissipation of the novel scheme. Moreover, the novel scheme demonstrated excellent robustness, allowing simulations of an intense storm featuring rapid phase-changes and heavy precipitation with the same time step as the second-order variant.

Overall, using the genuinely third-order accurate MPDATA consistently improved simulation results in a variety of benchmarks relevant to atmospheric modelling. The

improvement was significant not only when compared to the standard second-order MPDATA but also to the constant coefficient third-order variant. Because the option comes at about the same computational expense as its constant-coefficients predecessor, it is a valuable addition to the MPDATA based fluid-dynamics codes. Moreover, the use of fully third-order accurate MPDATA can be generally recommended for transport of tracers. Admittedly, it is not possible to make a similar recommendation for arbitrary fluid dynamics problems. While improvements by using the fully third-order scheme can be expected, the benefits may not outweigh the increased computational cost. This is the case especially when the problem is dominated by factors other than advection, such as strong forcings. Nevertheless, having the option for third-order accuracy allows numerical experimentation, possibly illuminating the impact of advection errors on a solution. In simulations of turbulent flows, the fully third-order accurate MPDATA is an interesting option due to its advantageous ILES properties. Finally, an increased complexity of the new scheme is offset by the general accessibility of its source code.

Appendices

A Detailed modified equation analysis of the standard MPDATA with two iterations

A.1 Expansion in space

By expanding the first iteration of MPDATA, $m = 1$ in (2.11), in Taylor series about a common spatial point $\boldsymbol{x_i}$ the following equation is obtained

$$\begin{aligned}\Psi^{(1)} = \Psi^n + \frac{\delta t}{G}\nabla\cdot\left\{-\boldsymbol{V}^{n+1/2}\Psi^n + \frac{\boldsymbol{\delta x}}{2}\odot\left|\boldsymbol{V}^{n+1/2}\right|\odot\nabla\Psi^n + \boldsymbol{H}_{UPW}\right\} \\ + O^4(\delta t, \boldsymbol{\delta x}), \\ \boldsymbol{H}_{UPW} = -\frac{\boldsymbol{\delta x}\odot\boldsymbol{\delta x}}{24}\odot\Big(\boldsymbol{V}^{n+1/2}\odot\nabla\odot\nabla\Psi^n + 2\nabla\Psi^n\odot\nabla\odot\boldsymbol{V}^{n+1/2} \\ + \Psi^n\nabla\odot\nabla\odot\boldsymbol{V}^{n+1/2}\Big),\end{aligned} \tag{A.1}$$

where the index $\boldsymbol{i}$ was omitted, because the resulting equation is valid for arbitrary $\boldsymbol{i}$. Similarly, expanding the second iteration, $m = 2$ in (2.11), under the assumption that the discrete approximations to the pseudo-velocity components at the staggered spatial grid points are at least second-order accurate, leads to

$$\Psi^{n+1} = \Psi^{(1)} + \frac{\delta t}{G}\nabla\cdot\left\{-\overline{\boldsymbol{V}}^{n+1/2,\,(1)}\Psi^{(1)} + \frac{\boldsymbol{\delta x}}{2}\odot\left|\overline{\boldsymbol{V}}^{n+1/2,\,(1)}\right|\odot\nabla\Psi^{(1)}\right\} + O^4(\delta t, \boldsymbol{\delta x}), \tag{A.2}$$

where a shorthand notation $\overline{\boldsymbol{V}}^{a,\,b} = \overline{\boldsymbol{V}}(\boldsymbol{V}^a, \Psi^b)$ was adopted.

Using the definition of pseudo-velocity (2.10) in the first term under the divergence operator on the rhs of (A.2) leaves

$$\begin{aligned}\Psi^{n+1} = \Psi^{(1)} + \frac{\delta t}{G}\nabla\cdot\Bigg\{-\frac{\boldsymbol{\delta x}}{2}\odot\left|\boldsymbol{V}^{n+1/2}\right|\odot\nabla\Psi^{(1)} + \frac{\delta t}{2G}\boldsymbol{V}^{n+1/2}\nabla\cdot\left(\boldsymbol{V}^{n+1/2}\Psi^{(1)}\right) \\ + \frac{\boldsymbol{\delta x}}{2}\odot\left|\overline{\boldsymbol{V}}^{n+1/2,\,(1)}\right|\odot\nabla\Psi^{(1)}\Bigg\} + O^4(\delta t, \boldsymbol{\delta x}).\end{aligned} \tag{A.3}$$

The elimination of $\Psi^{(1)}$ from (A.3) proceeds in two steps. First, (A.1) is used in the first term on the rhs of (A.3) which results in

$$\begin{aligned}\Psi^{n+1} = \Psi^n + \frac{\delta t}{G}\nabla\cdot\Bigg\{ &- \boldsymbol{V}^{n+1/2}\Psi^n - \frac{\boldsymbol{\delta x}}{2}\odot\left\uparrow \boldsymbol{V}^{n+1/2}\right\uparrow \odot(\nabla\Psi^{(1)} - \nabla\Psi^n)\\ &+ \frac{\delta t}{2G}\boldsymbol{V}^{n+1/2}\nabla\cdot\left(\boldsymbol{V}^{n+1/2}\Psi^{(1)}\right)\\ &+ \frac{\boldsymbol{\delta x}}{2}\odot\left\uparrow \overline{\boldsymbol{V}}^{n+1/2,\,(1)}\right\uparrow \odot\nabla\Psi^{(1)} + \boldsymbol{H}_{UPW}\Bigg\}\\ &+ O^4(\delta t, \boldsymbol{\delta x}).\end{aligned} \tag{A.4}$$

As (A.1) implies

$$\nabla\Psi^{(1)} = \nabla\Psi^n - \delta t\nabla\left[\frac{1}{G}\nabla\cdot\left(\boldsymbol{V}^{n+1/2}\Psi^n\right)\right] + O^2(\delta t, \boldsymbol{\delta x})\ , \tag{A.5}$$

$$\begin{aligned}\nabla\cdot\left(\boldsymbol{V}^{n+1/2}\Psi^{(1)}\right) = \nabla\cdot\left(\boldsymbol{V}^{n+1/2}\Psi^n\right) - \delta t\nabla\cdot\left[\frac{\boldsymbol{V}^{n+1/2}}{G}\nabla\cdot\left(\boldsymbol{V}^{n+1/2}\Psi^n\right)\right]\\ + O^2(\delta t, \boldsymbol{\delta x})\ ,\end{aligned} \tag{A.6}$$

after applying (A.1), (A.5) and (A.6) to the rhs of (A.4) the result reads

$$\begin{aligned}\Psi^{n+1} = \Psi^n + \frac{\delta t}{G}\nabla\cdot\left\{-\boldsymbol{V}^{n+1/2}\Psi^n + \frac{\delta t}{2G}\boldsymbol{V}^{n+1/2}\nabla\cdot\left(\boldsymbol{V}^{n+1/2}\Psi^n\right) + \boldsymbol{H}_X\right\}\\ + O^4(\delta t, \boldsymbol{\delta x})\ ,\end{aligned} \tag{A.7}$$

$$\begin{aligned}\boldsymbol{H}_X = \boldsymbol{H}_{UPW} &+ \frac{\boldsymbol{\delta x}}{2}\odot\left\uparrow \overline{\boldsymbol{V}}^{n+1/2,\,n}\right\uparrow \odot\nabla\Psi^n\\ &+ \frac{\delta t}{2}\boldsymbol{\delta x}\odot\left\uparrow \boldsymbol{V}^{n+1/2}\right\uparrow \odot\nabla\left[\frac{1}{G}\nabla\cdot\left(\boldsymbol{V}^{n+1/2}\Psi^n\right)\right]\\ &- \frac{\delta t^2}{2G}\boldsymbol{V}^{n+1/2}\nabla\cdot\left[\frac{\boldsymbol{V}^{n+1/2}}{G}\nabla\cdot\left(\boldsymbol{V}^{n+1/2}\Psi^n\right)\right].\end{aligned} \tag{A.8}$$

A.2 Expansion in time

By expanding (A.7) in time about a common time level t^n and again omitting its index, as the resulting equation is valid for arbitrary n, the following equation is obtained

$$\Psi + \delta t\frac{\partial \Psi}{\partial t} + \frac{\delta t^2}{2}\frac{\partial^2 \Psi}{\partial t^2} + \frac{\delta t^3}{6}\frac{\partial^3 \Psi}{\partial t^3} = \Psi + \frac{\delta t}{G}\nabla\cdot\Bigg\{ - \boldsymbol{V}\Psi - \frac{\delta t}{2}\frac{\partial \boldsymbol{V}}{\partial t}\Psi + \frac{\delta t}{2G}\boldsymbol{V}\nabla\cdot(\boldsymbol{V}\Psi) + \boldsymbol{H}_{TX}\Bigg\} + O^4(\delta t, \boldsymbol{\delta x}) \ , \tag{A.9}$$

$$\boldsymbol{H}_{TX} = \widetilde{\boldsymbol{H}_X} - \frac{\delta t^2}{8}\frac{\partial^2 \boldsymbol{V}}{\partial t^2}\Psi + \frac{\delta t^2}{4G}\frac{\partial \boldsymbol{V}}{\partial t}\nabla\cdot(\boldsymbol{V}\Psi) + \frac{\delta t^2}{4G}\boldsymbol{V}\nabla\cdot\left(\frac{\partial \boldsymbol{V}}{\partial t}\Psi\right) \ ,$$

where $\widetilde{\boldsymbol{H}_X}$ refers to (A.8) after time expansion that, for high order terms, amounts to replacing $\boldsymbol{V}^{n+1/2}$ with $\boldsymbol{V}^n$ and $\overline{\boldsymbol{V}}^{n+1/2,\,n}$ with $\overline{\boldsymbol{V}}^{n,\,n}$.

Finally, dividing both sides of (A.9) by δt and rearranging leads to the modified equation of MPDATA

$$\frac{\partial \Psi}{\partial t} = \frac{1}{G}\nabla\cdot\left\{-\boldsymbol{V}\Psi - \frac{\delta t}{2}\frac{\partial \boldsymbol{V}}{\partial t}\Psi + \frac{\delta t}{2G}\boldsymbol{V}\nabla\cdot(\boldsymbol{V}\Psi) + \boldsymbol{H}_{TX}\right\} - \frac{\delta t}{2}\frac{\partial^2 \Psi}{\partial t^2} - \frac{\delta t^2}{6}\frac{\partial^3 \Psi}{\partial t^3} + O^3(\delta t, \boldsymbol{\delta x}). \tag{A.10}$$

A.3 Expressing temporal derivatives in terms of spatial derivatives

In order to express the rhs of (A.10) solely in terms of the spatial derivatives of the scalar Ψ, the second and the third temporal derivative of Ψ have to be related to the spatial derivatives. First, by observing that the second temporal derivative on the rhs of (A.10) is multiplied by δt and the third is multiplied by δt^2, it follows that it is sufficient to know them up to $O^2(\delta t, \boldsymbol{\delta x})$ and $O^1(\delta t, \boldsymbol{\delta x})$, respectively. Keeping this in mind, differentiating (A.10) with respect to time results in

$$\frac{\partial^2 \Psi}{\partial t^2} = \frac{1}{G}\nabla\cdot\Bigg\{ - \frac{\partial \boldsymbol{V}}{\partial t}\Psi - \boldsymbol{V}\frac{\partial \Psi}{\partial t} - \frac{\delta t}{2}\frac{\partial^2 \boldsymbol{V}}{\partial t^2}\Psi - \frac{\delta t}{2}\frac{\partial \boldsymbol{V}}{\partial t}\frac{\partial \Psi}{\partial t} + \frac{\delta t}{2G}\frac{\partial \boldsymbol{V}}{\partial t}\nabla\cdot(\boldsymbol{V}\Psi) + \frac{\delta t}{2G}\boldsymbol{V}\nabla\cdot\left(\frac{\partial \boldsymbol{V}}{\partial t}\Psi\right) + \frac{\delta t}{2G}\boldsymbol{V}\nabla\cdot\left(\boldsymbol{V}\frac{\partial \Psi}{\partial t}\right)\Bigg\} - \frac{\delta t}{2}\frac{\partial^3 \Psi}{\partial t^3} + O^2(\delta t, \boldsymbol{\delta x}). \tag{A.11}$$

Using (A.10) on the rhs of (A.11) gives

$$\frac{\partial^2\Psi}{\partial t^2} = \frac{1}{G}\nabla\cdot\Bigg\{-\frac{\partial \boldsymbol{V}}{\partial t}\Psi + \frac{\boldsymbol{V}}{G}\nabla\cdot(\boldsymbol{V}\Psi) - \frac{\delta t}{2}\frac{\partial^2\boldsymbol{V}}{\partial t^2}\Psi - \frac{\delta t}{G}\boldsymbol{V}\nabla\cdot\left[\frac{\boldsymbol{V}}{G}\nabla\cdot(\boldsymbol{V}\Psi)\right] + \frac{\delta t}{2}\boldsymbol{V}\frac{\partial^2\Psi}{\partial t^2} + \frac{\delta t}{G}\frac{\partial \boldsymbol{V}}{\partial t}\nabla\cdot(\boldsymbol{V}\Psi) + \frac{\delta t}{G}\boldsymbol{V}\nabla\cdot\left(\frac{\partial \boldsymbol{V}}{\partial t}\Psi\right)\Bigg\} - \frac{\delta t}{2}\frac{\partial^3\Psi}{\partial t^3} + O^2(\delta t, \boldsymbol{\delta x})\ . \tag{A.12}$$

Applying (A.12) to the rhs of itself results in

$$\frac{\partial^2\Psi}{\partial t^2} = \frac{1}{G}\nabla\cdot\Bigg\{-\frac{\partial \boldsymbol{V}}{\partial t}\Psi + \frac{\boldsymbol{V}}{G}\nabla\cdot(\boldsymbol{V}\Psi) - \frac{\delta t}{2}\frac{\partial^2\boldsymbol{V}}{\partial t^2}\Psi - \frac{\delta t}{2G}\boldsymbol{V}\nabla\cdot\left[\frac{\boldsymbol{V}}{G}\nabla\cdot(\boldsymbol{V}\Psi)\right] + \frac{\delta t}{G}\frac{\partial \boldsymbol{V}}{\partial t}\nabla\cdot(\boldsymbol{V}\Psi) + \frac{\delta t}{2G}\boldsymbol{V}\nabla\cdot\left(\frac{\partial \boldsymbol{V}}{\partial t}\Psi\right)\Bigg\} - \frac{\delta t}{2}\frac{\partial^3\Psi}{\partial t^3} + O^2(\delta t, \boldsymbol{\delta x}). \tag{A.13}$$

Differentiating (A.13) with respect to time and using the order argument again gives

$$\frac{\partial^3\Psi}{\partial t^3} = \frac{1}{G}\nabla\cdot\Bigg\{-\frac{\partial^2 \boldsymbol{V}}{\partial t^2}\Psi - \frac{\partial \boldsymbol{V}}{\partial t}\frac{\partial\Psi}{\partial t} + \frac{1}{G}\frac{\partial \boldsymbol{V}}{\partial t}\nabla\cdot(\boldsymbol{V}\Psi) + \frac{\boldsymbol{V}}{G}\nabla\cdot\left(\frac{\partial \boldsymbol{V}}{\partial t}\Psi\right) + \frac{\boldsymbol{V}}{G}\nabla\cdot\left(\boldsymbol{V}\frac{\partial\Psi}{\partial t}\right)\Bigg\} + O^1(\delta t, \boldsymbol{\delta x}). \tag{A.14}$$

Using (A.10) on the rhs of (A.14) leads to

$$\frac{\partial^3\Psi}{\partial t^3} = \frac{1}{G}\nabla\cdot\Bigg\{-\frac{\partial^2 \boldsymbol{V}}{\partial t^2}\Psi + \frac{2}{G}\frac{\partial \boldsymbol{V}}{\partial t}\nabla\cdot(\boldsymbol{V}\Psi) + \frac{\boldsymbol{V}}{G}\nabla\cdot\left(\frac{\partial \boldsymbol{V}}{\partial t}\Psi\right) - \frac{\boldsymbol{V}}{G}\nabla\cdot\left[\frac{\boldsymbol{V}}{G}\nabla\cdot(\boldsymbol{V}\Psi)\right]\Bigg\} + O^1(\delta t, \boldsymbol{\delta x}). \tag{A.15}$$

Applying first (A.13) and then (A.15) to the rhs of (A.10) leaves

$$\frac{\partial\Psi}{\partial t} = \frac{1}{G}\nabla\cdot\{-\boldsymbol{V}\Psi + \boldsymbol{H}_{XX}\} + O^3(\delta t, \boldsymbol{\delta x}), \tag{A.16}$$

$$\boldsymbol{H}_{XX} = \boldsymbol{H}_{TX} + \frac{\delta t^2}{6}\frac{\partial^2\boldsymbol{V}}{\partial t^2}\Psi - \frac{\delta t^2}{3G}\frac{\partial \boldsymbol{V}}{\partial t}\nabla\cdot(\boldsymbol{V}\Psi) - \frac{\delta t^2}{6G}\boldsymbol{V}\nabla\cdot\left(\frac{\partial \boldsymbol{V}}{\partial t}\Psi\right) + \frac{\delta t^2}{6G}\boldsymbol{V}\nabla\cdot\left[\frac{\boldsymbol{V}}{G}\nabla\cdot(\boldsymbol{V}\Psi)\right]\ . \tag{A.17}$$

Finally, the definition $\overline{\overline{\boldsymbol{V}}} := \boldsymbol{H}_{XX}/\Psi$ leads to the final result (3.10) with $\alpha = 1$, $\beta_M = 1$ and $\gamma = 1$.

B Warm-rain microphysics

Here, the standard warm-rain microphysics (Kessler, 1969; Grabowski and Smolarkiewicz, 1996) used in supercell simulations of Chapter 7 is summarised. In the following, all formulae with numeral coefficients assume SI units.

Following Klemp and Wilhelmson (1978), the precipitation terminal velocity is prescribed as

$$w_t = 36.34(10^{-3}\rho q_p)^{0.1364}(\rho/\rho_0)^{-1/2}, \tag{B.1}$$

where ρ_0 is the density at the ground level.

In (7.2) – (7.4), the bulk condensation rate C_d is defined implicitly by assuming that the water vapour is saturated in the presence of cloud water

$$q_c > 0 \implies q_v = q_{vs}, \tag{B.2}$$

and that the cloud water evaporates instantaneously in subsaturated conditions

$$q_v < q_{vs} \implies q_c = 0. \tag{B.3}$$

The saturated water vapour mixing ratio is given by

$$q_{vs} = \frac{\epsilon e_s}{p - e_s}, \tag{B.4}$$

where $\epsilon = R_d/R_v$ and the saturation water vapour pressure is

$$e_s(T) = e_0 \exp\left[\frac{L}{R_v}\left(\frac{1}{T_0} - \frac{1}{T}\right)\right], \tag{B.5}$$

with $e_0 = 611$ Pa and $T_0 = 273.16$ K. Other microphysical sources on the rhs of (7.2) – (7.6) are given by the power law expressions

$$A_p = \max\left(0, k_1(q_c - q_c^T)\right), \tag{B.6}$$

$$C_p = k_2 q_c q_p^{0.875}, \tag{B.7}$$

$$E_p = \frac{1}{\rho}\frac{(q_v/q_{vs} - 1)C(10^{-3}\rho q_p)^{0.525}}{5.4 \times 10^2 + 2.55 \times 10^5/(pq_{vs})}, \tag{B.8}$$

where $k_1 = 10^{-3}\,\mathrm{s}^{-1}$, $k_2 = 2.2\,\mathrm{s}^{-1}$, $q_c = 10^{-4}\,\mathrm{kg\,kg}^{-1}$ and $C = 1.6{+}124.9(10^{-3}\rho q_p)^{0.2046}$ is the ventilation factor. Here, the autoconversion threshold q_c^T was chosen to be 10^{-3} kg kg^{-1}.

Bibliography

Arabas, S., D. Jarecka, A. Jaruga, and M. Fijałkowski, 2014: Formula Translation in Blitz++, NumPy and Modern Fortran: A Case Study of the Language Choice Tradeoffs. *Sci. Programming*, **22**, 201–222, doi:10.3233/SPR-140379.

Arabas, S., A. Jaruga, H. Pawlowska, and W. W. Grabowski, 2015: libcloudph++ 1.0: a single-moment bulk, double-moment bulk, and particle-based warm-rain microphysics library in C++. *Geosci. Model Dev.*, **8**, 1677–1707, doi:10.5194/gmd-8-1677-2015.

Brown, D. L., and M. L. Minion, 1995: Performance of under-resolved two-dimensional incompressible flows simulations. *J. Comput. Phys.*, **122**, 165–183, doi:10.1006/jcph.1995.1205.

Carmichael, G. R., A. Sandu, T. Chai, D. N. Daescu, E. M. Constantinescu, and Y. Tang, 2008: Predicting air quality: Improvements through advanced methods to integrate models and measurements. *J. Comput. Phys.*, **227**, 3540–3571, doi:10.1016/j.jcp.2007.02.024.

Chorin, A. J., 1967: A numerical method for solving incompressible viscous flow problems. *J. Comput. Phys.*, **2**, 12–26, doi:10.1016/0021-9991(67)90037-X.

Cossette, J.-F., P. Charbonneau, P. K. Smolarkiewicz, and M. P. Rast, 2017: Magnetically modulated heat transport in a global simulation of solar magneto-convection. *Astrophys. J.*, **841**, 65–81, doi:10.3847/1538-4357/aa6d60.

Domaradzki, J. A., Z. Xiao, and P. K. Smolarkiewicz, 2003: Effective eddy viscosities in implicit large eddy simulations of turbulent flows. *Phys. Fluids*, **15**, 3890–3893, doi:10.1063/1.1624610.

Drikakis, D., L. Margolin, and P. K. Smolarkiewicz, 2002: On 'spurious' eddies. *Int. J. Numer. Methods Fluids*, **40**, 313–322, doi:10.1002/fld.288.

Drikakis, D., and P. K. Smolarkiewicz, 2001: On spurious vortical structures. *J. Comput. Phys.*, **172**, 309–325, doi:10.1006/jcph.2001.6825.

Frohn, L. M., J. H. Christensen, and J. Brandt, 2002: Development of a high-resolution nested air pollution model: The numerical approach. *J. Comput. Phys.*, **179**, 68–94, doi:10.1006/jcph.2002.7036.

Ghizaru, M., P. Charbonneau, and P. K. Smolarkiewicz, 2010: Magnetic cycles in global large-eddy simulations of solar convection. *Astrophys. J. Lett.*, **715**, L133–L137, doi:10.1088/2041-8205/715/2/L133.

Grabowski, W. W., and P. K. Smolarkiewicz, 1996: Two-time-level semi-Lagrangian modeling of precipitating clouds. *Mon. Weather Rev.*, **124**, 487–497, doi:10.1175/1520-0493(1996)124<0487:TTLSLM>2.0.CO;2.

Gross, E. S., L. Bonaventura, and G. Rosatti, 2002: Consistency with continuity in conservative advection schemes for free-surface models. *Int. J. Numer. Methods Fluids*, **38**, 307–327, doi:10.1002/fld.222.

Gustafsson, B., H.-O. Kreiss, and J. Oliger, 1995: *Time dependent problems and difference methods*, Vol. 24. John Wiley & Sons.

Hundsdorfer, W., B. Koren, van Loon M., and J. G. Verwer, 1995: A positive finite-difference advection scheme. *J. Comput. Phys.*, **117**, 35–46, doi:10.1006/jcph.1995.1042.

Hürsch, W. L., and C. V. Lopes, 1995: Separation of Concerns. Tech. rep.

Ince, D. C., L. Hatton, and J. Graham-Cumming, 2012: The case for open computer programs. *Nature*, **482**, 485, doi:10.1038/nature10836.

Jarecka, D., A. Jaruga, and P. K. Smolarkiewicz, 2015: A spreading drop of shallow water. *J. Comput. Phys.*, **289**, 53–61, doi:10.1016/j.jcp.2015.02.003.

Jaruga, A., S. Arabas, D. Jarecka, H. Pawlowska, P. K. Smolarkiewicz, and M. Waruszewski, 2015: libmpdata++ 1.0: a library of parallel MPDATA solvers for systems of generalised transport equations. *Geosci. Model Dev.*, **8**, 1005–1032, doi:10.5194/gmd-8-1005-2015.

Kelly, J. F., and F. X. Giraldo, 2012: Continuous and discontinuous Galerkin methods for a scalable three-dimensional nonhydrostatic atmospheric model: Limited-area mode. *J. Comput. Phys.*, **231**, 7988–8008, doi:10.1016/j.jcp.2012.04.042.

Kessler, E., 1969: On the distribution and continuity of water substance in atmospheric circulations. *On the distribution and continuity of water substance in atmospheric circulations*, Springer, 1–84, doi:10.1007/978-1-935704-36-2_1.

Klemp, J., W. Skamarock, and S.-H. Park, 2015: Idealized global nonhydrostatic atmospheric test cases on a reduced-radius sphere. *J. Adv. Model. Earth Sy.*, **7**, 1155–1177, doi:10.1002/2015MS000435.

Klemp, J. B., 1987: Dynamics of tornadic thunderstorms. *Annu. Rev. Fluid Mech.*, **19**, 369–402, doi:10.1146/annurev.fl.19.010187.002101.

Klemp, J. B., and R. B. Wilhelmson, 1978: The simulation of three-dimensional convective storm dynamics. *J. Atmos. Sci.*, **35**, 1070–1096, doi:10.1175/1520-0469(1978)035<1070:TSOTDC>2.0.CO;2.

Knoll, D. A., L. Chacon, L. G. Margolin, and V. A. Mousseau, 2003: On balanced approximations for time intergation of multiple time scale systems. *J. Comput. Phys.*, **185**, 583–611, doi:10.1016/S0021-9991(03)00008-1.

Kreiss, H.-O., and J. Oliger, 1972: Comparison of accurate methods for the integration of hyperbolic equations. *Tellus*, **24**, 199–215, doi:10.1111/j.2153-3490.1972.tb01547.x.

Kühnlein, C., W. Deconinck, R. Klein, S. Malardel, Z. P. Piotrowski, P. K. Smolarkiewicz, J. Szmelter, and N. P. Wedi, 2018: FVM 1.0: A nonhydrostatic finite-volume dynamical core formulation for IFS. *Geosci. Model Dev. Discuss.*, **2018**, 1–37, doi:10.5194/gmd-2018-237.

Kühnlein, C., and P. K. Smolarkiewicz, 2017: An unstructured-mesh finite-volume MPDATA for compressible atmospheric dynamics. *J. Comput. Phys.*, **334**, 16–30, doi:10.1016/j.jcp.2016.12.054.

Kühnlein, C., P. K. Smolarkiewicz, and A. Dörnbrack, 2012: Modelling atmospheric flows with adaptive moving meshes. *J. Comput. Phys.*, **231**, 2741–2763, doi:10.1016/j.jcp.2011.12.012.

Kumar, D., R. Bhattacharyya, and P. K. Smolarkiewicz, 2015: Repetitive formation and decay of current sheets in magnetic loops: An origin of diverse magnetic structures. *Phys. Plasmas*, **22**, 012 902, doi:10.1063/1.4905643.

Kurowski, M., B. Rosa, and M. Ziemiański, 2011: Testing the anelastic nonhydrostatic model EULAG as a prospective dynamical core of a numerical weather prediction model Part II: Simulations of supercell. *Acta Geophys.*, **59**, 1267–1293, doi:10.2478/s11600-011-0051-z.

Kurowski, M. J., W. W. Grabowski, and P. K. Smolarkiewicz, 2014: Anelastic and compressible simulation of moist deep convection. *J. Atmos. Sci.*, **71**, 3767–3787, doi:10.1175/JAS-D-14-0017.1.

Lauritzen, P. H., W. C. Skamarock, M. J. Prather, and M. A. Taylor, 2012: A standard test case suite for two-dimensional linear transport on the sphere. *Geosci. Model Dev.*, **5**, 887–901, doi:10.5194/gmd-5-887-2012.

Lauritzen, P. H., and J. Thuburn, 2012: Evaluating advection/transport schemes using interrelated tracers, scatter plots and numerical mixing diagnostics. *Q. J. R. Meteorol. Soc.*, **138**, 906–918, doi:10.1002/qj.986.

Lauritzen, P. H., and Coauthors, 2014: A standard test case suite for two-dimensional linear transport on the sphere: results from a collection of state-of-the-art schemes. *Geosci. Model Dev.*, **7**, 105–145, doi:10.5194/gmd-7-105-2014.

Lax, P., and B. Wendroff, 1960: Systems of conservation laws. *Commun. Pure Appl. Math.*, **13**, 217–237, doi:10.1002/cpa.3160130205.

Margolin, L., and P. K. Smolarkiewicz, 1998: Antidiffusive velocities for multipass donor cell advection. *SIAM J. Sci. Comput.*, **20**, 907–929, doi:10.1137/S106482759324700X.

Margolin, L. G., and W. J. Rider, 2002: A rationale for implicit turbulence modelling. *Int. J. Numer. Methods Fluids*, **39**, 821–841, doi:10.1002/fld.331.

Margolin, L. G., W. J. Rider, and F. F. Grinstein, 2006a: Modeling turbulent flow with implicit LES. *J. Turb.*, **7**, 1–27, doi:10.1080/14685240500331595.

Margolin, L. G., P. K. Smolarkiewicz, and Z. Sorbjan, 1999: Large-eddy simulations of convective boundary layers using nonoscillatory differencing. *Physica D*, **133**, 390–397, doi:10.1016/S0167-2789(99)00083-4.

Margolin, L. G., P. K. Smolarkiewicz, and A. A. Wyszogradzki, 2006b: Dissipation in implicit turbulence models: A computational study. *J. Appl. Mech.*, **73**, 469–473, doi:10.1115/1.2176749.

Margolin, L. G., P. K. Smolarkiewicz, and A. A. Wyszogrodzki, 2002: Implicit turbulence modeling for high Reynolds number flows. *J. Fluids Eng.*, **124**, 862–867, doi:10.1115/1.1514210.

Merali, Z., 2010: Computational science: Error, why scientific programming does not compute. *Nature*, **467**, 775–777, doi:10.1038/467775a.

Minion, M. L., and D. L. Brown, 1997: Performance of under-resolved two-dimensional incompressible flows simulations II. *J. Comput. Phys.*, **138**, 734–765, doi:10.1006/jcph.1997.5843.

Morin, A., J. Urban, P. Adams, I. Foster, A. Sali, D. Baker, and P. Sliz, 2012: Shining light into black boxes. *Science*, **336**, 159–160, doi:10.1126/science.1218263.

Nair, R. D., and C. Jablonowski, 2008: Moving vortices on the sphere: A test case for horizontal advection problems. *Mon. Weather Rev.*, **136**, 699–711, doi:10.1175/2007MWR2105.1.

Piotrowski, Z. P., P. K. Smolarkiewicz, S. P. Malinowski, and A. A. Wyszogrodzki, 2009: On numerical realizability of thermal convection. *J. Comput. Phys.*, **228**, 6268–6290, doi:10.1016/j.jcp.2009.05.023.

Pope, S. B., 2000: Turbulent Flows. Cambridge University Press.

Prusa, J. M., P. K. Smolarkiewicz, and A. A. Wyszogrodzki, 2008: EULAG, a computational model for multiscale flows. *Comput. Fluids*, **37**, 1193–1207, doi:10.1016/j.compfluid.2007.12.001.

Pudykiewicz, J., 1989: Simulation of the Chernobyl dispersion with a 3-D hemispheric tracer model. *Tellus B*, **41**, 391–412, doi:10.1111/j.1600-0889.1989.tb00317.x.

Pudykiewicz, J. A., 1998: Application of adjoint tracer transport equations for evaluating source parameters. *Atmos. Environ.*, **32**, 3039–3050, doi:10.1016/S1352-2310(97)00480-9.

Racine, É., P. Charbonneau, M. Ghizaru, A. Bouchat, and P. K. Smolarkiewicz, 2011: On the mode of dynamo action in a global large-eddy simulation of solar convection. *Astrophys. J.*, **735**, 46–67, doi:10.1088/0004-637X/735/1/46.

Richtmyer, R. D., and K. W. Morton, 1967: Difference methods for initial-value problems. Second edition. John Wiley & Sons.

Roache, P. J., 1972: Computational Fluid Dynamics. Hermosa Publishers.

Roache, P. J., 2002: Code verification by the method of manufactured solutions. *J. Fluids Eng.*, **124**, 4–10, doi:10.1115/1.1436090.

Santillana, M., L. Zhang, and R. Yantosca, 2016: Estimating numerical errors due to operator splitting in global atmospheric chemistry models: Transport and chemistry. *J. Comput. Phys.*, **305**, 372–386, doi:10.1016/j.jcp.2015.10.052.

Schmidt, H., and U. Schumann, 1989: Coherent structure of the convective boundary layer derived from large-eddy simulations. *J. Fluid. Mech.*, **200**, 511–562, doi:10.1017/S0022112089000753.

Skamarock, W. C., J. B. Klemp, M. G. Duda, L. D. Fowler, S.-H. Park, and T. D. Ringler, 2012: A multiscale nonhydrostatic atmospheric model using centroidal Voronoi tesselations and C-grid staggering. *Mon. Weather Rev.*, **140**, 3090–3105, doi:10.1175/MWR-D-11-00215.1.

Smolarkiewicz, P., and L. Margolin, 2000: Variational methods for elliptic problems in fluid models. *Proc. ECMWF Workshop on Developments in numerical methods for very high resolution global models*, 137–159.

Smolarkiewicz, P. K., 1983: A simple positive definite advection scheme with small implicit diffusion. *Mon. Weather Rev.*, **111**, 479–486, doi:10.1175/1520-0493(1983)111<0479:ASPDAS>2.0.CO;2.

Smolarkiewicz, P. K., 1984: A fully multidimensional positive definite advection transport algorithm with small implicit diffusion. *J. Comput. Phys.*, **54**, 325–362, doi:10.1016/0021-9991(84)90121-9.

Smolarkiewicz, P. K., 2006: Multidimensional positive definite advection transport algorithm: An overview. *Int. J. Numer. Methods Fluids*, **50**, 1123–1144, doi:10.1002/fld.1071.

Smolarkiewicz, P. K., and P. Charbonneau, 2013: EULAG, a computational model for multiscale flows: An MHD extension. *J. Comput. Phys.*, **236**, 608–623, doi:10.1016/j.jcp.2012.11.008.

Smolarkiewicz, P. K., and T. L. Clark, 1986: The multidimensional positive definite advection transport algorithm: further development and applications. *J. Comput. Phys.*, **67**, 396–438, doi:10.1016/0021-9991(86)90270-6.

Smolarkiewicz, P. K., W. Deconinck, M. Hamrud, C. Kühnlein, G. Mozdzynski, J. Szmelter, and N. P. Wedi, 2016: A finite-volume module for simulating global all-scale atmospheric flows. *J. Comput. Phys.*, **314**, 287–304, doi:10.1016/j.jcp.2016.03.015.

Smolarkiewicz, P. K., and W. W. Grabowski, 1990: The multidimensional positive definite advection transport algorithm: Nonoscillatory option. *J. Comput. Phys.*, **86**, 355–375, doi:10.1016/0021-9991(90)90105-A.

Smolarkiewicz, P. K., C. Kühnlein, and W. W. Grabowski, 2017: A finite-volume module for cloud-resolving simulations of global atmospheric flows. *J. Comput. Phys.*, **341**, 208–229, doi:10.1016/j.jcp.2017.04.008.

Smolarkiewicz, P. K., C. Kühnlein, and N. P. Wedi, 2014: A consistent framework for discrete integrations of soundproof and compressible PDEs of atmospheric dynamics. *J. Comput. Phys.*, **263**, 185–205, doi:10.1016/j.jcp.2014.01.031.

Smolarkiewicz, P. K., and L. G. Margolin, 1993: On forward-in-time differencing for fluids: Extension to a curvilinear framework. *Mon. Weather Rev.*, **121**, 1847–1859, doi:10.1175/1520-0493(1993)121<1847:OFITDF>2.0.CO;2.

Smolarkiewicz, P. K., and L. G. Margolin, 1998: MPDATA: A finite-difference solver for geophysical flows. *J. Comput. Phys.*, **140**, 459–480, doi:10.1006/jcph.1998.5901.

Smolarkiewicz, P. K., and J. Szmelter, 2005: MPDATA: An edge-based unstructured-grid formulation. *J. Comput. Phys.*, **206**, 624–649, doi:10.1016/j.jcp.2004.12.021.

Smolarkiewicz, P. K., and J. Szmelter, 2011: A nonhydrostatic unstructured-mesh soundproof model for simulation of internal gravity waves. *Acta Geophys.*, **59**, 1109, doi:10.2478/s11600-011-0043-z.

Smolarkiewicz, P. K., J. Szmelter, and A. A. Wyszogrodzki, 2013: An unstructured-mesh atmospheric model for nonhydrostatic dynamics. *J. Comput. Phys.*, **254**, 184–199, doi:10.1016/j.jcp.2013.07.027.

Strang, G., 1968: On the construction and comparison of difference schemes. *SIAM J. Numer. Anal.*, **5**, 506–517, doi:10.1137/0705041.

Strugarek, A., P. Beaudoin, A. S. Brun, P. Charbonneau, S. Mathis, and P. K. Smolarkiewicz, 2016: Modeling turbulent stellar convection zones: Sub-grid scales effects. *Adv. Space Res.*, **58**, 1538–1553, doi:10.1016/j.asr.2016.05.043.

Sullivan, P. P., and E. G. Patton, 2011: The effect of mesh resolution on convective boundary layer statistics and structures generated by large-eddy simulation. *J. Atmos. Sci.*, **68**, 2395–2415, doi:10.1175/JAS-D-10-05010.1.

Szmelter, J., and P. K. Smolarkiewicz, 2010: An edge-based unstructured mesh discretisation in geospherical framework. *J. Comput. Phys.*, **229**, 4980–4995, doi:10.1016/j.jcp.2010.03.017.

The Sage Developers, 2018: *SageMath, the Sage Mathematics Software System (Version 8.4.0)*. `http://www.sagemath.org`.

Thuburn, J., 2008: Some conservation issues for the dynamical cores of nwp and climate models. *J. Comput. Phys.*, **227**, 3715–3730, doi:10.1016/j.jcp.2006.08.016.

Toro, E. F., 2009: Riemann solvers and numerical methods for fluid dynamics: a practical introduction. Third edition. Springer-Verlag.

Ullrich, P. A., 2014: Understanding the treatment of waves in atmospheric models. Part 1: The shortest resolved waves of the 1D linearized shallow-water equations. *Q. J. R. Meteorol. Soc.*, **140**, 1426–1440, doi:10.1002/qj.2226.

Ullrich, P. A., and C. Jablonowski, 2012: MCore: A non-hydrostatic atmospheric dynamical core utilizing high-order finite-volume methods. *J. Comput. Phys.*, **231**, 5078–5108, doi:10.1016/j.jcp.2012.04.024.

Ullrich, P. A., and Coauthors, 2017: DCMIP2016: a review of non-hydrostatic dynamical core design and intercomparison of participating models. *Geosci. Model Dev.*, **10**, 4477–4509, doi:10.5194/gmd-10-4477-2017.

Wang, Z. J., and Coauthors, 2013: High-order CFD methods: current status and perspective. *Int. J. Numer. Methods Fluids*, **72**, 811–845, doi:10.1002/fld.3767.

Warming, R. F., and B. J. Hyett, 1974: The modified equation approach to the stability and accuracy analysis of finite-difference methods. *J. Comput. Phys.*, **14**, 159–179, doi:10.1016/0021-9991(74)90011-4.

Warn-Varnas, A., J. Hawkins, P. K. Smolarkiewicz, S. A. Chin-Bing, D. King, and Z. Hallock, 2007: Solitary wave effects north of Strait of Messina. *Ocean Model.*, **18**, 97–121, doi:10.1016/j.ocemod.2007.03.003.

Waruszewski, M., C. Kühnlein, H. Pawlowska, and P. K. Smolarkiewicz, 2018: MPDATA: Third-order accuracy for variable flows. *J. Comput. Phys.*, **359**, 361–379, doi:10.1016/j.jcp.2018.01.005.

White III, J. B., and J. J. Dongarra, 2011: High-performance high-resolution semi-Lagrangian tracer transport on a sphere. *J. Comput. Phys.*, **230**, 6778–6799, doi:10.1016/j.jcp.2011.05.008.

Wilson, G., and Coauthors, 2014: Best practices for scientific computing. *PLoS biol.*, **12**, e1001 745, doi:10.1371/journal.pbio.1001745.

Zalesak, S. T., 1979: Fully multidimensional flux-corrected transport algorithms for fluids. *J. Comput. Phys.*, **31**, 335–362, doi:10.1016/0021-9991(79)90051-2.

Zarzycki, C. M., and Coauthors, 2018: DCMIP2016: The Splitting Supercell Test Case. *Geosci. Model Dev. Discuss.*, doi:10.5194/gmd-2018-156.